CHAPTER 4

A TERMINAL FE^{III}-OXO IN A TETRANUCLEAR CLUSTER: EFFECTS OF DISTAL METAL CENTERS ON STRUCTURE AND REACTIVITY

The text for this chapter was reproduced in part from:

Reed, C. J.; Agapie, T. *J. Am. Chem. Soc.*., **2019**, *Accepted Manuscript.* doi:10.1021/jacs.9b03157

ABSTRACT

Tetranuclear Fe clusters have been synthesized bearing a terminal Fe^{III}-oxo center stabilized by hydrogen bonding interactions from pendant *tert*-butyl amino pyrazolate ligands. This motif was supported in multiple Fe oxidation states, ranging from $[Fe^{II}_2Fe^{III}_2]$ to $[Fe^{III}_4]$; two oxidation states were structurally characterized by single crystal X-ray diffraction. The reactivity of the Fe^{III}-oxo center in proton coupled electron transfer (PCET) with X–H (X = C, O) bonds of various strengths was studied in conjunction with analysis of thermodynamic square schemes of the cluster oxidation states. These results demonstrate the important role adjacent metal centers have on modulating the reactivity of a terminal metal-oxo.

INTRODUCTION

Terminal metal-oxo moieties are invoked as key intermediates in both natural and synthetic catalysts of mid-first-row transition metal ions (Mn, Fe, and Co).[1] For example in photosynthesis, water is oxidized in photosystem II by a $CaMn_4O_5$ cluster known as the oxygen evolving complex (OEC);[2] numerous computational studies of the catalytic mechanism have proposed a high-valent Mn-oxo playing a key role in O–O bond formation.[3] Similarly, a number of synthetic water oxidation catalysts employing various multinuclear scaffolds have been reported, where a terminal metal-oxo is implicated as a key intermediate (Figure 1).[1e-g, 4]

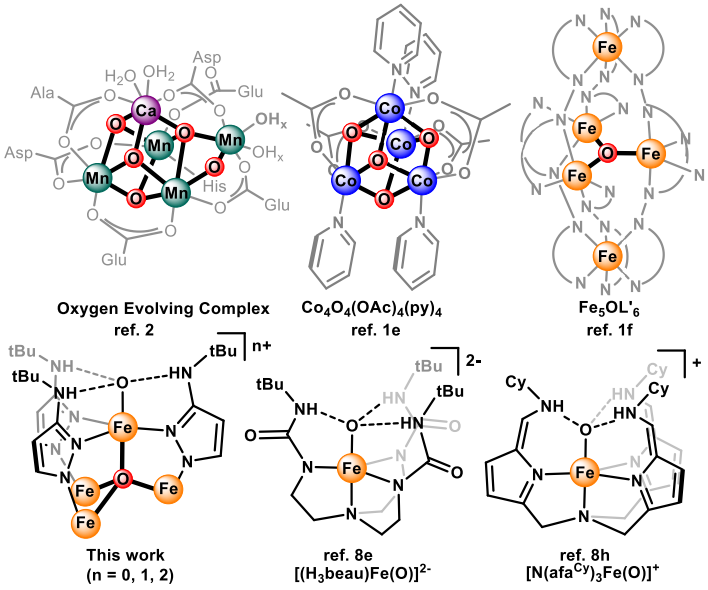

Figure 1. Multinuclear catalysts with proposed terminal metal-oxo intermediates (top), and structurally characterized terminal Fe^{III}-oxo complexes (bottom).

Studies of synthetic transition metal-oxo complexes have been integral for understanding these reactive moieties in catalytic systems.[1a, 5] However, there is a paucity of literature concerning multinuclear complexes bearing well-characterized terminal metal-oxo motifs.[6] In a rare example where the effects of a neighboring metal oxidation state on a terminal metal-oxo could be interrogated, Que and coworkers reported that the spin state of an Fe^{IV}-oxo

center would change depending on the oxidation state of a neighboring Fe in a μ_2-O bridged bimetallic complex ($L'_2OFe_2(OH)(O)^{2+/3+}$).[6c] The authors demonstrated that structural and spin-state changes due to reduction of this secondary Fe leads to a thousand-fold activation of the [Fe_2] complex towards C–H oxidation.

To gain further insight into these multimetallic effects, previous group members, Dr. Graham de Ruiter and Kurtis Carsch, studied the reactivity of Fe_4, Fe_3Mn, and Mn_4 clusters, bearing aryl-substituted pyrazolate ligands, towards oxygen atom transfer reagents; in all cases, intramolecular C–H (or C–F) activation occurs, forming a five-coordinate apical metal with a phenoxypyrazolate donor.[7] Analysis of the reaction mechanism were consistent with rate-limiting iodosylarene activation step, producing a transient reactive moiety (either iodosylarene adduct or terminal-oxo) that could not be directly observed. Inspired by reports of mononuclear terminal metal-oxo motifs stabilized by second coordination sphere hydrogen bonding interactions,[8] our group has previously used this strategy to access a terminal Mn^{III}–OH moiety as part of a [Mn_4] cluster.[9] Dr. Kyle Horak was able to serendipitously isolate the analogous Fe cluster, **[$LFe_3O(PzNHPh)_3Fe(OH)$][OTf]**, however, there were challenges with accessing this cluster in reasonable purity and yield.[10] Due to the observed difficulties in supporting clusters with the amino-phenylpyrazolate ligand, new amino-pyrazolate donors were investigated. Herein, we describe the synthesis, structural characterization, and reactivity studies of clusters bearing a terminal Fe^{III}-oxo motif, stabilized by *tert*-butyl-amino-pyrazolates, to probe the significance of a multinuclear scaffold on structural and reactivity aspects of a terminal metal-oxo.

Scheme 1. Previous Efforts Towards Isolation of a Terminal Metal-Oxo in a Multinuclear System by the Agapie Group

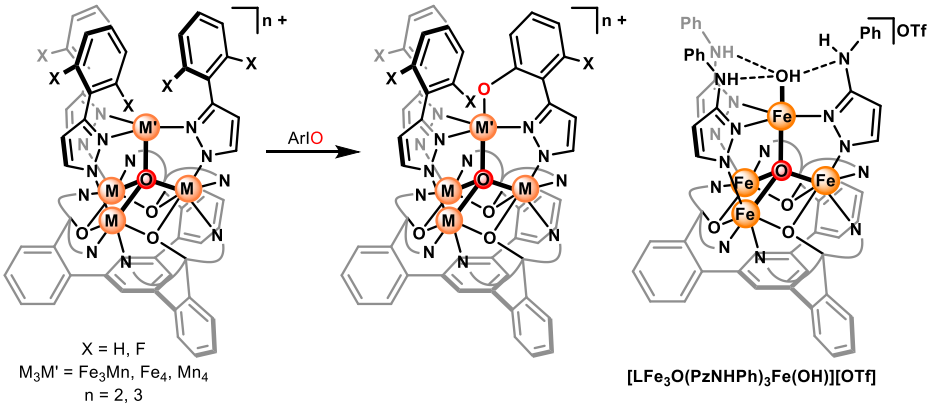

RESULTS AND DISCUSSION

Synthesis of Fe_4-Hyroxide and Fe_4-Oxo Clusters. Treatment of the reported **$LFe_3(OAc)(OTf)_2$** cluster (OTf, triflate = trifluoromethane sulfonate)[11] with three equivalents of potassium *tert*-butyl-amino-pyrazolate (KPzNHtBu) and iodosylbenzene (PhIO), followed by addition of iron (II) triflate bis-acetonitrile ($Fe(OTf)_2$ • 2 MeCN) and excess potassium hydroxide in tetrahydrofuran (THF) produces the neutral [$Fe^{II}_3Fe^{III}$] cluster, **1** (Scheme 2). Single crystal X-ray diffraction (XRD) studies of **1** reveal a structure similar to our previously reported [Mn_4] cluster bearing a terminal hydroxide ligand (Figure 2);[9] the apical metal displays a trigonal bipyramidal geometry, with the terminal hydroxide ligand hydrogen bonded to each amino-pyrazolate (N–O distances of 2.826(1), 2.765(1), 2.789(1) Å for **1**). The relatively short distance between the apical Fe and the interstitial μ_4-O (Fe4–O1), 1.837(1) Å, is consistent with an Fe^{III} in the apical position of the cluster, with the remaining Fe centers being Fe^{II}.[7a, 12]

Scheme 2. Synthesis of [Fe$_4$] clusters. (Inset) 1,3,5-triarylbenzene ligand (L^{3-}) and *tert*-butyl amino pyrazolate ligand (PzNHtBu$^-$).

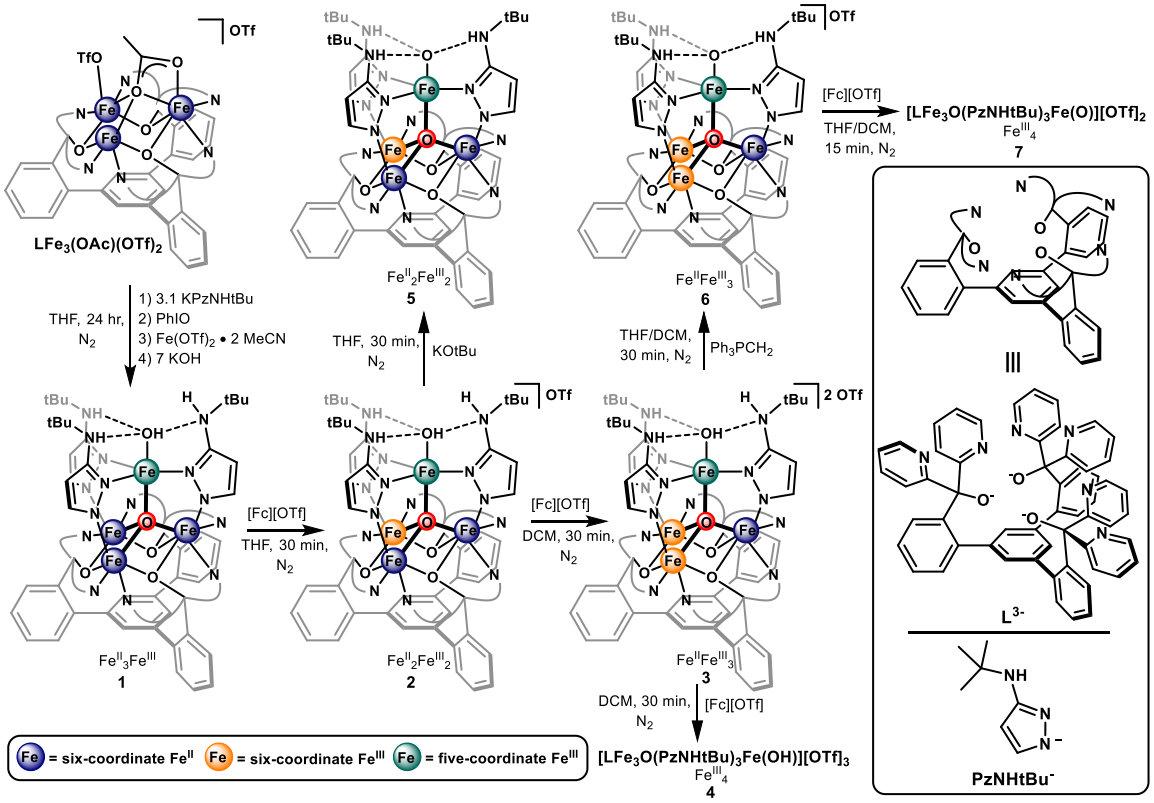

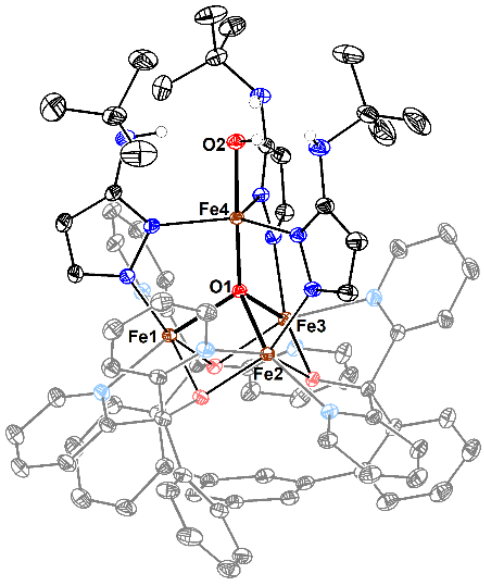

Figure 2. Crystal structure of **1**. Ellipsoids are shown at the 50% probability level. Hydrogen atoms and solvent molecules removed for clarity.

The electrochemistry of the [Fe_4] hydroxide clusters in THF features three quasi-reversible events assigned to the [$Fe^{II}_3Fe^{III}$]→[$Fe^{II}_2Fe^{III}_2$] (-1.53 V; all potentials vs. Fc/Fc^+), [$Fe^{II}_2Fe^{III}_2$]→[$Fe^{II}Fe^{III}_3$] (-0.68 V), and [$Fe^{II}Fe^{III}_3$]→[Fe^{III}_4] (-0.10 V) redox couples (Figure 3). Each of the corresponding oxidation states of the cluster could be isolated (Scheme 1). Mössbauer spectra of the oxidized clusters **2**, **3**, and **4** are consistent with oxidations occurring at the Fe^{II} centers in the tri-iron core and the Fe–OH moiety remaining Fe^{III} (Figure 4 and Table 1).

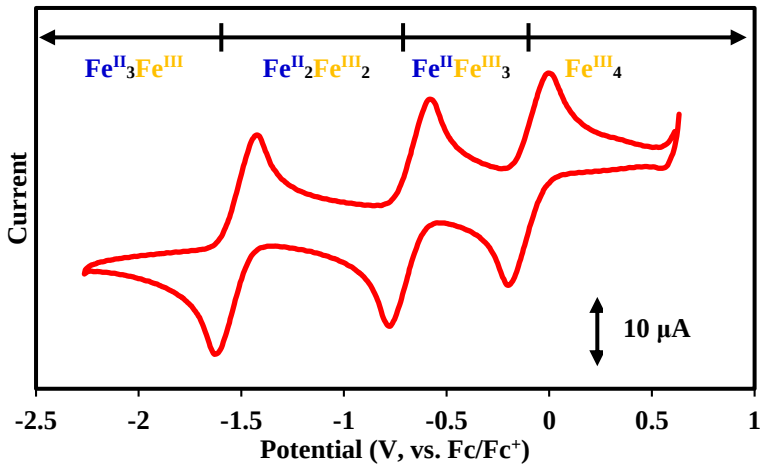

Figure 3. Cyclic voltammetry of **2**, (2.5 mM) at 50 mV/s in THF with a glassy carbon working, platinum counter, and silver wire reference electrodes and ca. 200 mM [Bu_4N][PF_6].

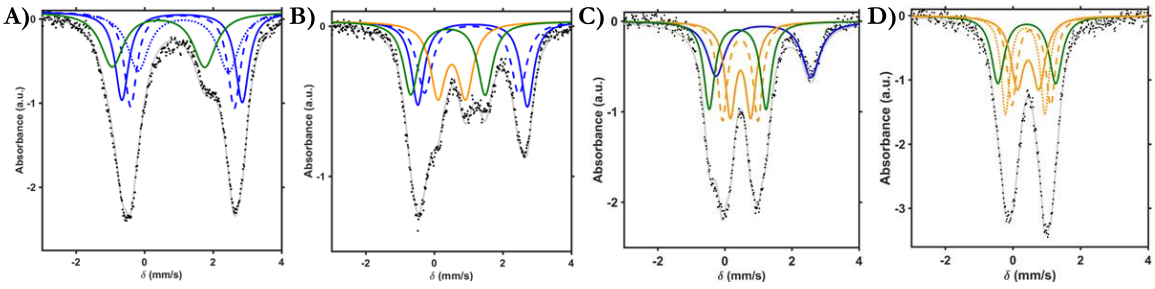

Figure 4. Mössbauer spectra of (A) **1**, (B) **2**, (C) **3**, and (D) **4**; see parameters in Table 1.

Table 1. ^{57}Fe Mössbauer Parameters for Complexes 1 – 4.

	δ (mm/s)	$\|\Delta E_q\|$ (mm/s)	assign-ment
1 ($Fe^{II}_3Fe^{III}$)			
Fe1, Fe2, Fe3	1.10, 1.11, 1.13	3.52, 3.03, 2.64	*h.s.* Fe^{II}
Fe4	0.41	2.71	apical Fe^{III}
2 ($Fe^{II}_2Fe^{III}_2$)			
Fe1, Fe2	1.12, 1.10	3.20, 2.76	*h.s.* Fe^{II}
Fe3	0.52	0.81	*h.s.* Fe^{III}
Fe4	0.41	2.17	apical Fe^{III}
3 ($Fe^{II}Fe^{III}_3$)			
Fe1	1.15	2.83	*h.s.* Fe^{II}
Fe2, Fe3	0.47, 0.46	0.61, 1.06	*h.s.* Fe^{III}
Fe4	0.38	1.69	apical Fe^{III}
4 (Fe^{III}_4)			
Fe1, Fe2, Fe3	0.45, 0.53, 0.36	0.64, 1.15, 1.17	*h.s.* Fe^{III}
Fe4	0.41	1.71	*a*pical Fe^{III}

Access to a terminal Fe^{III}-oxo moiety was achieved by deprotonation of the $[Fe^{II}_2Fe^{III}_2]$ hydroxide cluster, **2**, with potassium *tert*-butoxide (KO*t*Bu; Scheme 1). The resulting compound, **5**, was crystallographically characterized (Figure 5); deprotonation of the hydroxide ligand leads to structural changes to the apical Fe in **5**. The Fe4–O2 distance contracts to 1.817(2) Å, compared to the distances in **1** (1.937(1) Å) and the precursor **2** (1.907(3) Å); this bond length matches closely with the structurally characterized Fe^{III}-oxo complexes reported by Borovik and Fout.[8e, 8h, 8i] Compound **6**, prepared by deprotonating **3**, also displays a short Fe4–O2 distance (1.795(8) Å). Furthermore, the apical Fe-μ_4-O distance (Fe4–O1) elongates to 1.965(2) Å in **5** and 2.049(7) Å in **6**, from 1.890(3) Å in **2** and 1.948(2) Å in **3**, which is consistent with a greater trans influence exerted by the terminal oxo ligand. Terminal Fe^{III}-oxo complexes are rare, and typically stabilized through hydrogen bonding interactions.[8e, 8h, 8i, 13] The structures of **5** and **6** display comparable hydrogen bonding distances

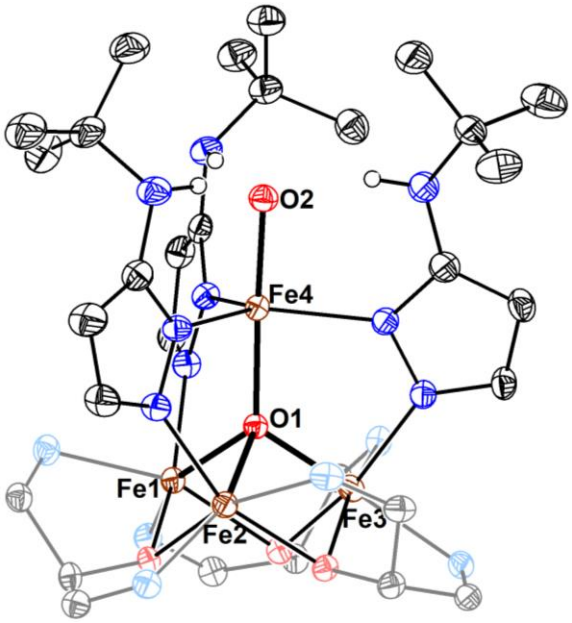

Figure 5. Truncated crystal structure of Fe^{III}-oxo cluster, **5**. Hydrogen atoms and solvent molecules removed for clarity.

Table 2. Selected Bond Distances and Angles, Structural Index Parameter, and Mössbauer Parameters of Reported Fe^{III}-Oxo Complexes

	5	**6**	**$[(H_3beau)Fe(O)]^{2-}$** [8e]	**$[N(afa^{Cy})_3Fe(O)]^{+}$** [8h]
Fe–O (Å)	1.817(2)	1.795(8)	1.813(3)	1.806(1)
$Fe–N_{equatorial}$ (Å)	2.104(2), 2.098(2), 2.093(2)	2.100(8), 2.085(9), 2.087(9)	2.030(4), 2.060(4), 2.082(4)	2.049(1), 2.049(1), 2.052(1)
$Fe–L_{trans}$ (Å)	1.965(2) ($L=O^{2-}$)	2.049(7) ($L=O^{2-}$)	2.271(4) ($L=NR_3$)	2.276(1) ($L=NR_3$)
N–O (H-bond; Å)	2.647, 2.717, 2.685	2.718, 2.790, 2.750	2.732, 2.702, 2.686	2.641, 2.645, 2.673
$\angle N_{equatorial}–Fe–O$ (°)	96.3, 92.8, 92.0	93.6, 97.5, 96.3	103.3, 99.7, 100.8	102.6, 103.1, 103.1
$Fe–N\|N'\|N''_{equatorial}$ (Å)	0.14	0.22	0.42	0.45
Structural Index Parameter (τ)[a]	0.9	0.8	0.5	0.4
Mossbauer parameters (mm/s)	$\delta = 0.43$, $\|\Delta E_q\| = 3.04$	$\delta = 0.47$, $\|\Delta E_q\| = 2.53$	$\delta = 0.30$, $\|\Delta E_q\| = 0.91$	-

[a] $\tau = [\Sigma (\angle N_{equit.}–Fe–N'_{equit.}) - \Sigma (\angle N_{equit.}–Fe–O)]/90$

to other structurally characterized Fe^{III}-oxo complexes, **$[(H_3beau)Fe(O)]^{2-}$** and **$[N(afa^{Cy})_3Fe(O)]^{+}$**, along with similar equatorial Fe–N distances (Table 2). However, the μ_4-O distances in **5** (1.965(2) Å) and **6** (2.049(7) Å) are significantly shorter than the Fe–N

distances for the amine trans to the oxo in the mononuclear systems (~2.27 Å). This is likely a result of greater ligand flexibility in the mononuclear systems; the geometry of these Fe^{III}-oxo complexes display greater deviations from ideal trigonal bipyramidal geometry compared to the apical Fe in **5** and **6**, based on a structural index parameter (τ; ideal trigonal bipyramidal geometry = 1.0). For the clusters reported here, the rigid geometry of the pyrazolate ligands prevents significant distortion of the apical Fe out of the equatorial plane.

Electronic Structure Investigations of Tetranuclear Fe Clusters. The ^{57}Fe Mössbauer spectra of the Fe^{III}-oxo clusters **5** – **7** display relatively unique parameters for the apical Fe, relative to the structurally related Fe^{III}-oxo, where Mössbauer parameters have been reported, **$[(H_3beau)Fe(O)]^{2-}$** (Table 2 and Figure 4).[8e, 14] For example, the Mössbauer parameters assigned to the apical Fe of **5**, δ = 0.43 mm/s and $|\Delta E_Q|$ = 3.04 mm/s, are atypical for high-spin (S= 5/2) Fe^{III} centers, which typically display low quadrupole splitting values. A detailed examination of the electronic structure of the Fe_4 clusters was conducted through magnetic susceptibility measurements and EPR spectroscopy.

Variable temperature, and vaeriable temperature variable field, magnetic susceptibility measusurements were conducted on a series of the thermally stable Fe_4-hydroxide clusters (**2**

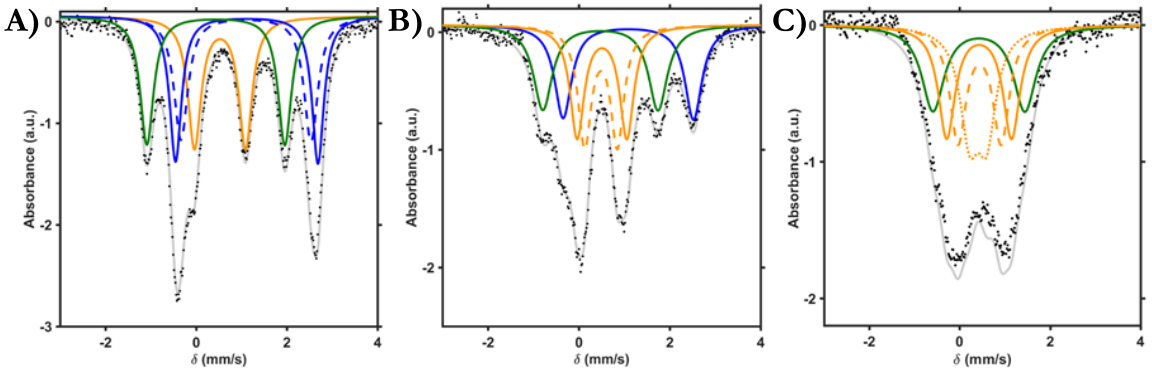

Figure 4. Zero applied-field Mössbauer spectra of (A) **5**, (B) **6**, and (C) **7**. The parameters of each doublet are listed in Table 3.

Table 3. ^{57}Fe Mössbauer Parameters for Complexes 5 – 7.

	δ (mm/s)	$\|\Delta E_q\|$ (mm/s)	assign-ment
5 ($Fe^{II}_3Fe^{III}$)			
Fe1, Fe2	1.12, 1.10	3.14, 2.87	*h.s.* Fe^{II}
Fe3	0.52	1.13	*h.s.* Fe^{III}
Fe4	0.43	3.04	apical Fe^{III}
6 ($Fe^{II}_2Fe^{III}_2$)			
Fe1	1.09	2.87	*h.s.* Fe^{II}
Fe2, Fe3	0.51, 0.49	1.09, 0.72	*h.s.* Fe^{III}
Fe4	0.47	2.53	apical Fe^{III}

	δ (mm/s)	$\|\Delta E_q\|$ (mm/s)	assign-ment
7 (Fe^{III}_4)			
Fe1, Fe2, Fe3	0.43, 0.44, 0.41	1.44, 0.95, 0.38	*h.s.* Fe^{III}
Fe4	0.43	2.03	apical Fe^{III}

– **4**) to establish their electronic ground states (Figure 5) The variable temperature magnetic susceptibility data for these compounds is consistent with high-spin Fe centers composing all cluster redox states for the series; the best fit for each complex is obtained by using exclusively S = 2 Fe^{II} and S = 5/2 Fe^{III}. The spin coupling model for these clusters is similar to that of structurally related high-spin Fe clusters bearing bridging imidazolate ligands, where strong antiferromagnetic coupling between the apical Fe^{III} and the tri-iron core promotes in ferromagnetic alignment of the spins with the remaining three Fe centers (Figure 5B).[12] The variable temperature variable field magnetization data for these compounds can be fit adequately using this coupling scheme, supporting assignments for spin ground states of S = 4, 9/2, and 5 for **2**, **3**, and **4**, respectively (Figure 6). The presence of increasing zero field splitting as **4** is reduced to **3** and **2** is observed in the magnetization data, causing saturation below the expected 2S limit (10 for **4**, 9 for **3**, and 8 for **2**).

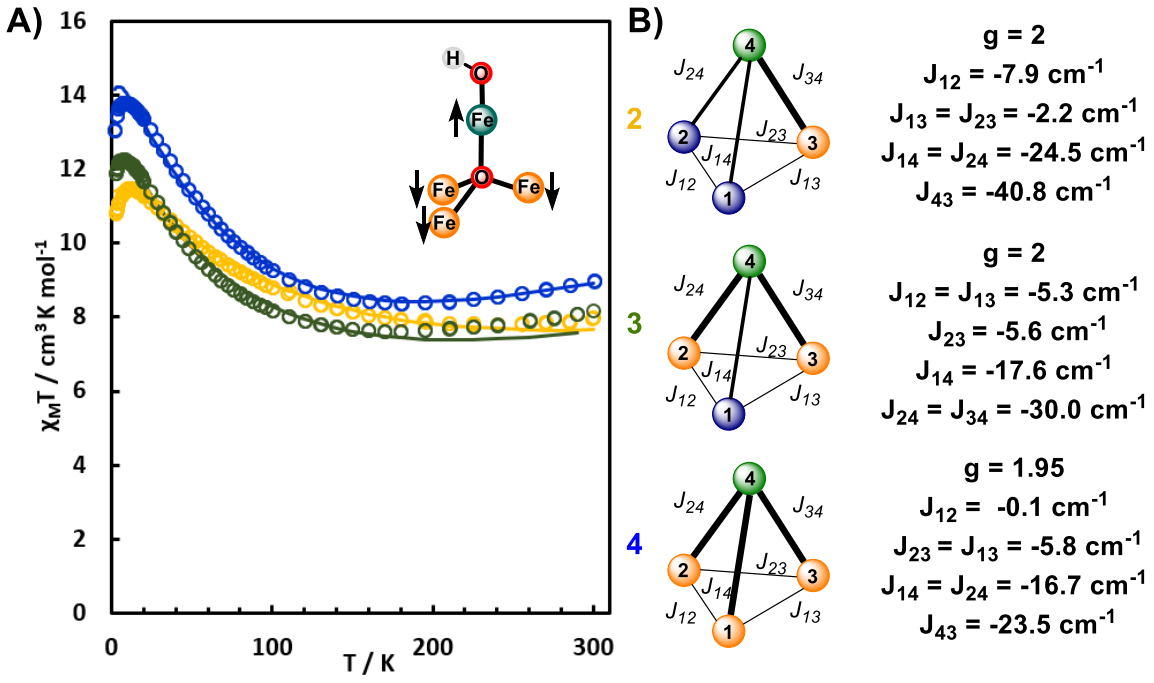

Figure 5. (A) Variable temperature direct current magnetic susceptibility data for Fe4-hydroxide clusters **2** (yellow), **3** (green), and **4** (blue) at 0.1 T. The spin coupling model has strong antiferromagnetic alignment of the apical Fe and the tri-iron core. (B) Simulation of coupling scheme for **2** – **4**, with all metal centers locally high spin.

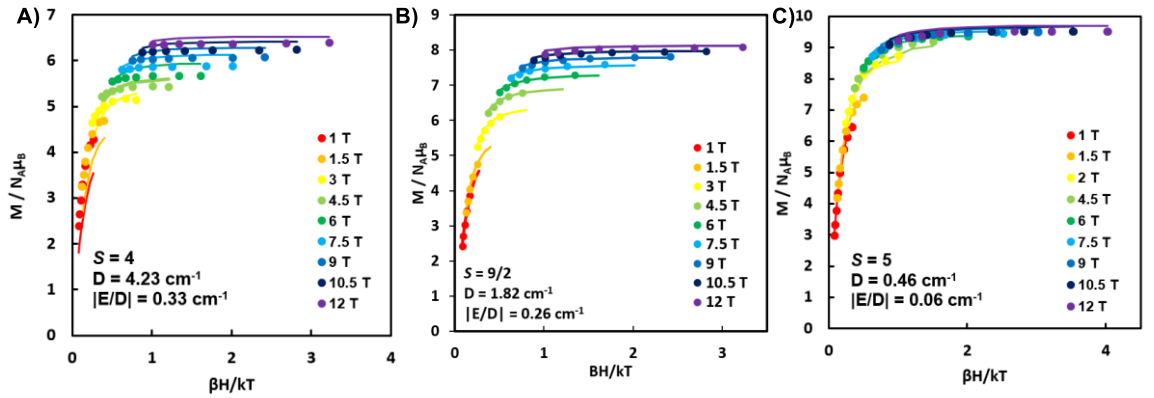

Figure 6. Variable temperature-variable field magnetization data for **2** (A), **3** (B), and **4** (D) from 2.5 K to 8 K. The spin and zero field splitting parameters (S, D, and |E/D|) were used to simulate the data.

Continuous wave EPR spectra of these paramagnetic clusters at low temperature (< 20 K) in frozen solutions display a number of features in regions expected for these high-spin systems (g >16). Figure 7 summarizes the parallel (for integer spin clusters **2**, **4**, **5**, and **7**) and perpendicular (for **3** and **6**) mode data collected. Attempts to simulate these spectra were challenging, even for the complexes where magnetization data was obtained. For example, **2** displays a sharp peak at ca. g = 17 at low temperatures (<15 K), which can be tentatively assigned to the $M_s = \pm 4$ doublet transition (Figure 7A).[12] In contrast, the corresponding $[Fe^{III}_2Fe^{II}_2]$ Fe-oxo cluster, **5**, displays one major transition near g ~ 19, which is consistent with an $S = 4$ or 5 system (Figure 7B). Further studies will examine the field-dependent Mössbauer spectra of these clusters to identify their spin ground states. Even without simulating the EPR data, there are noticable differences for each cluster oxidation state between Fe_4-hydroxide and –oxo, demonstrating the strong influence of the apical ligand on the electronics of the cluster.

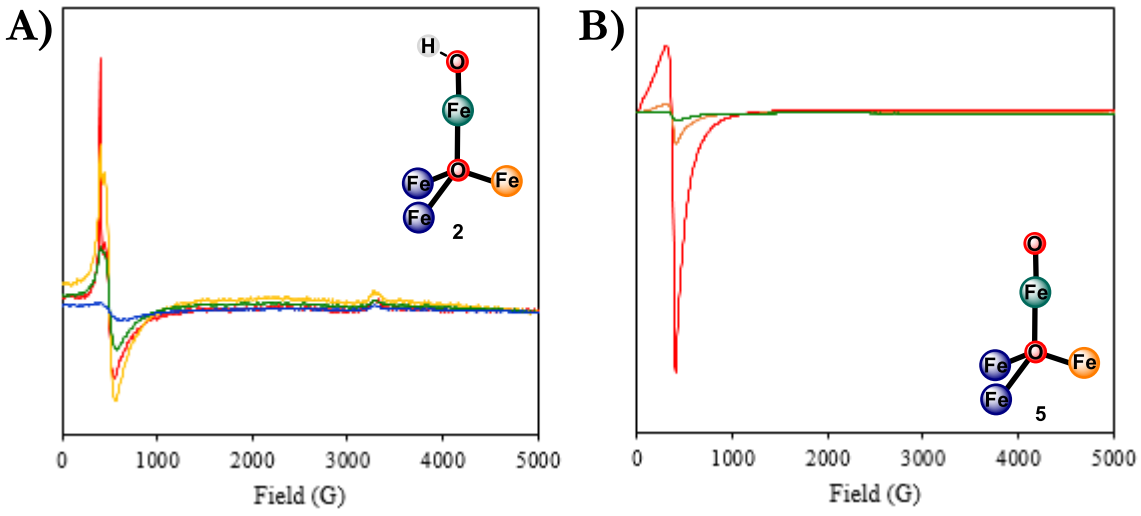

Figure 7. Parallel-mode EPR spectrum in 2-MeTHF of(A) **2** collected at 5 K (red), 10 K (orange), 15 K (green), and 25 K (blue), and (B) **5** at 5 K (red), 10 K (orange), and 15 K (green).

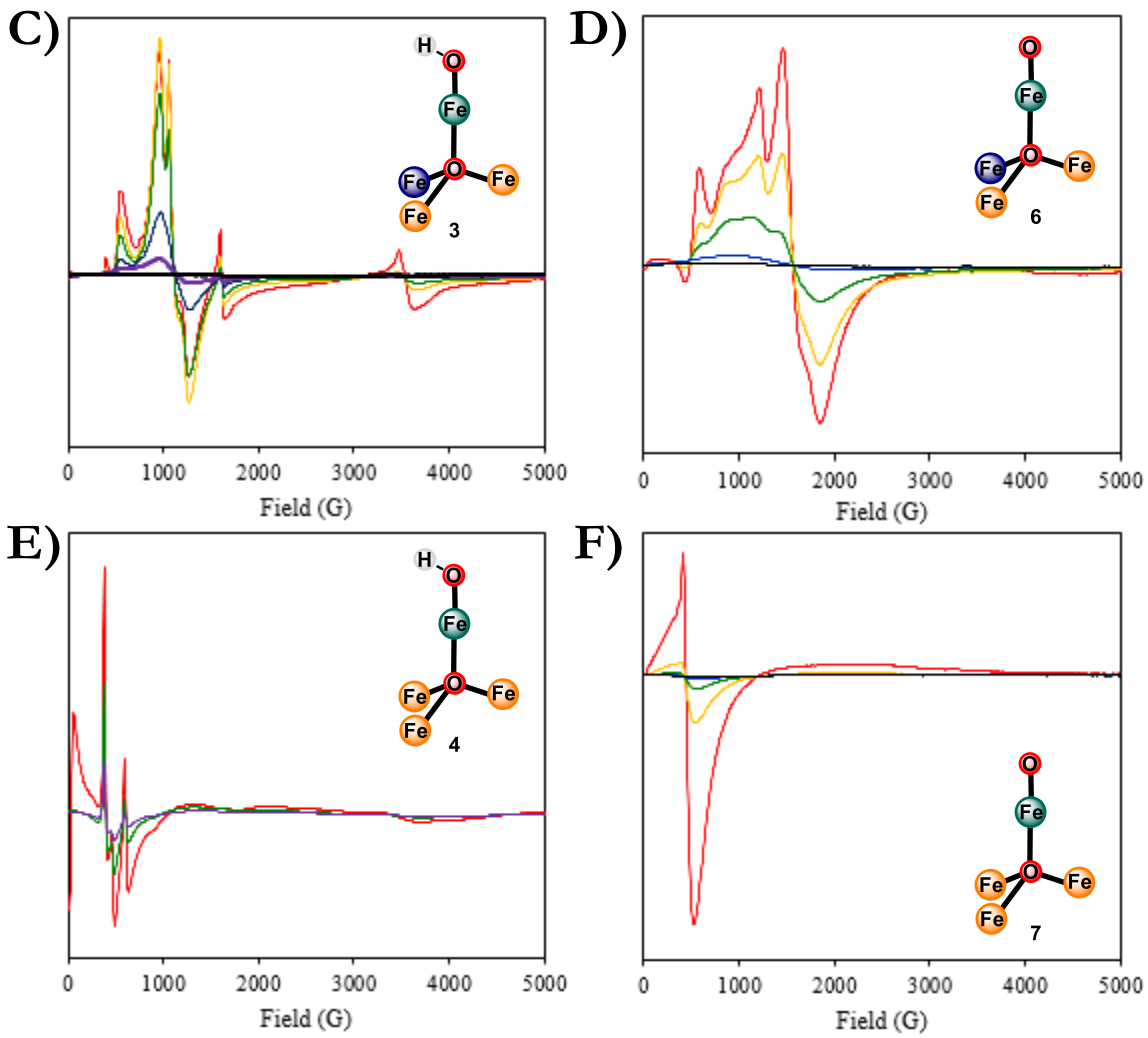

Figure 7 cont. (C) Perpendicular-mode CW-EPR spectrum of **3** collected in EtCN/PrCN at 5 K (red), 7.5 K (orange), 10 K (green), 15 K (blue), 20 K (purple), and 30 K (black). (D) Perpendicular-mode spectrum of **6** collected in EtCN/PrCN at 5 K (red), 7.5 K (orange), 10 K (green), 15 K (blue), and 20 K (black). (E) Parallel-mode spectrum of **4** in EtCN/PrCN at 5 K (red), 10 K (green), and 15 K (purple). (F) Parallel-mode spectrum of **7** in EtCN/PrCN at 5 K (red), 10 K (orange), 15 K (green), and 20 K (black).

---

pK_a and BDE$_{O-H}$ Determination for Fe$_4$-Hydroxide Clusters. The hydroxide ligand in **2** was determined to be very basic in THF (pK_a = 30.1; Table 4). Analogous equilibrium studies were performed on **3** and, as expected, oxidation of the cluster reduces the basicity of the

Fe^{III}-oxo moiety (pK_a = 23.0 for **3**; Table 5). Attempts to deprotonate **4** with various bases, even at low temperatures, only resulted in decomposition, so a pK_a value for this oxidation state was not measured. These data were combined with electrochemical information for clusters **1** (vide supra) and **5** (Figure 8), to produce thermodynamic square schemes according to equation 1 (Figure 9): [15]

$$BDE_{O-H} = 23.06\ E° + 1.37\ pK_a + C \qquad (1)$$

Table 4. pK_a determination of 2 via ^{31}P NMR spectroscopy.[a]

NMR	Equiv. Ph_3PCH_2	Equiv. $[Ph_3PCH_2]^+$	[**5**]/[**2**]	K^b
2 + 1.3 Ph_3PCH_2	~ 1.3	-	n.d.	n.d.
2 + 5 Ph_3PCH_2	4.54	0.46	0.85	0.09
2 + 7 Ph_3PCH_2	6.38	0.62	1.63	0.16
2 + 10 Ph_3PCH_2	9.24	0.76	3.17	0.26
2 + 18 Ph_3PCH_2	16.97	1.03	n.d.	n.d.
			Average *K*	0.17 (±0.09)

[a]The ratio of **2** to **5** was estimated from the relative integrals of the ^{31}P NMR peaks for Ph_3PCH_2 (~15 ppm) and $Ph_3PCH_3^+$ (~18 ppm); it was assumed that the equivalents of $[Ph_3PCH_3]^+$ produced in the NMR were due to partial deprotonation of **2**, and corresponded to equivalents of **5** ([$[Ph_3PCH_3][OTf]$] = [**5**]). [b]An equilibrium constant was determined according to the equation below:

$$K = \frac{[\mathbf{5}][[Ph_3PCH_3][OTf]]}{[\mathbf{2}][Ph_3PCH_2]}$$

where this value, along with the reported pK_a of Ph_3PCH_2 in THF, 29.3, was used to obtain a pK_a value of 30.1 (±1.0) for **2**.[16]

Table 5. pK_a determination of 3 via ^{1}H NMR spectroscopy

NMR	Equiv. **3**[a]	Equiv. **6**[a]	K^b
3 + 1 $tBuP_1$(pyrr)	0.55	0.45	0.70
3 + 5 $tBuP_1$(pyrr)	0.27	0.73	0.46
3 + 10 $tBuP_1$(pyrr)	0.12	0.88	0.71
		Average *K*	0.62 (±0.14)

[a]The ratio of **3** to **6** was based on the relative integrals of the ^{1}H NMR peaks at 17.0 (for **3**) and 14.5 ppm (for **6**); the relative amounts of base and conjugate acid of *tert*-butylimino-tri(pyrrolidino)phosphorene ($tBuP_1$(pyrr)) were assumed based on mass balance. [b]An equilibrium constant was determined according to the equation below:

$$K = \frac{[\mathbf{6}][[H'tBuP_1(pyrr)'][OTf]]}{[\mathbf{3}]['tBuP_1(pyrr)']}$$

where this value, along with the reported pK_a of $tBuP_1$(pyrr) in THF, 22.8, was used to obtain a pK_a value of 23.0 (±1.0) for **3**.[16]

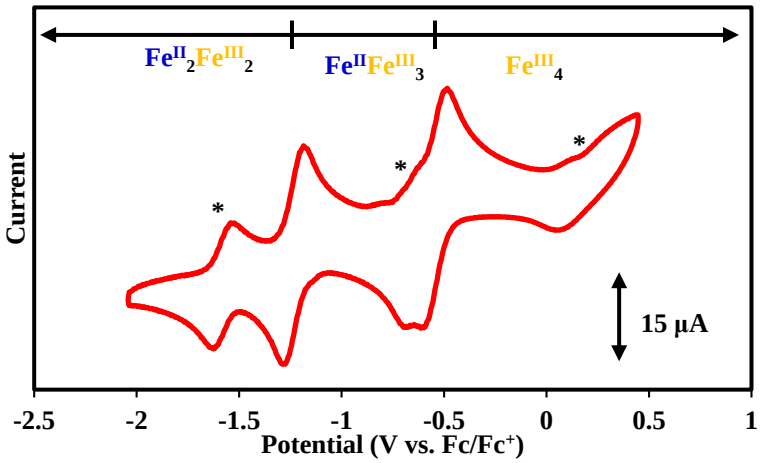

Figure 8. Cyclic voltammetry of **5** (2.3 mM at 200 mV/s scan rate) in THF with a glassy carbon working, platinum counter, and silver wire reference electrodes and ca. 100 mM $[Bu_4N][PF_6]$. Electrochemical events marked with an asterisk (*) are assigned to a small amount of $[LFe_3O(PzNHtBu)_3Fe(OH)]^{n+}$ that formed due to decomposition.

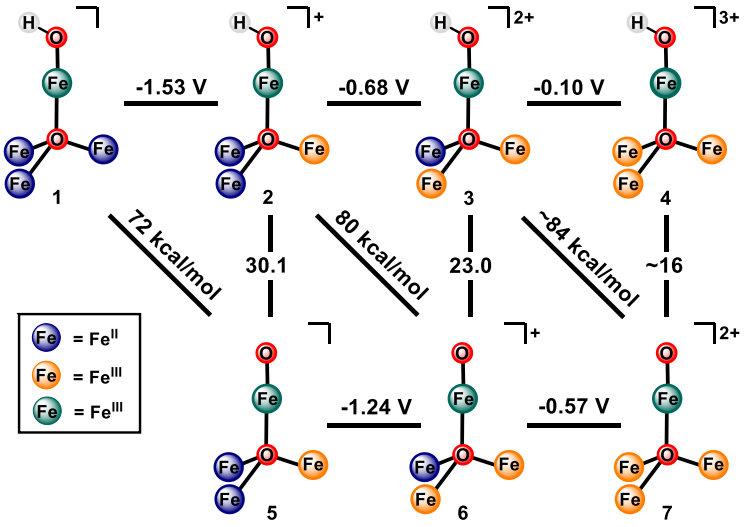

Figure 9. Thermodynamic cycles to evaluate the BDE_{O-H} values of the hydroxide clusters **1** – **3**. Reduction potentials (horizontal lines) are references to Fc/Fc^+. pK_a values (vertical lines) are based on relative pK_a values of cationic acids in THF. Diagonal lines are the BDE_{O-H} values calculated from these parameters according to the Bordwell equation (eq 1). Approximate values (~) have been extrapolated from the Bordwell equation.

Similar to our previously reported studies on [Fe_3Mn] hydroxide and aquo clusters, the bond dissociation enthalpy of the O–H bond ($BDE_{O–H}$) increases upon oxidation of the distal Fe centers, ranging from 72 kcal/mol in **1** to 84 kcal/mol in **3**.[17]

Reactivity Studies of Fe_4-Oxo Clusters. The three distal Fe oxidation states have a dramatic effect on the reactivity of the Fe^{III}-oxo center through modifying the pK_a and $BDE_{O–H}$ values. For example, **5** is incapable of performing proton coupled electron transfer (PCET) reactions[18,19] with substituted phenols over a range of phenol $BDE_{O–H}$ values (79 – 85 kcal/mol); only proton transfer to generate **2** is observed as expected from the combination of low $BDE_{O–H}$ for **1** and high pK_a of **2.** Oxidation of the remote Fe centers in **6** and **7** enables PCET reactivity with these phenols, resulting in the formation of **2** and **3**, respectively (Figure 10).

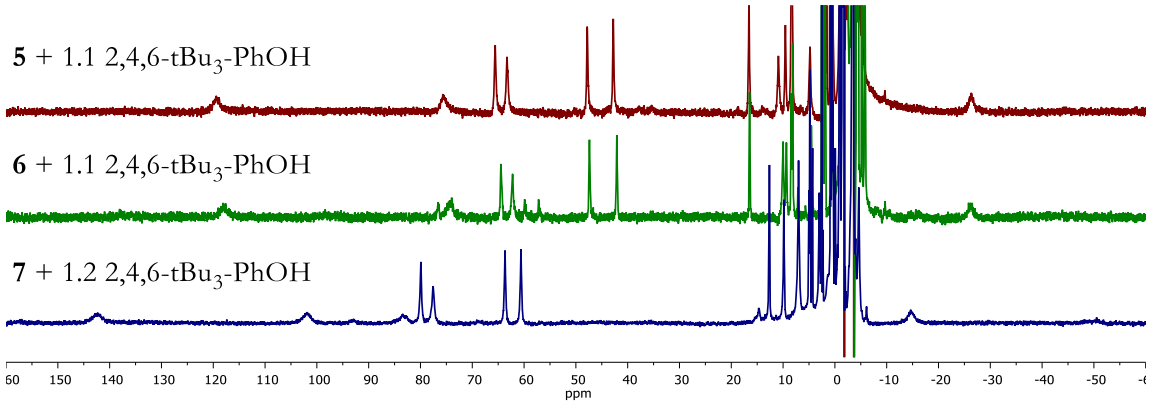

Figure 10. ^{1}H NMR spectra (400 MHz) in THF/C_6D_6 of reaction products with **5** - **7** and 2,4,6-tri-*tert*-butyl phenol (2,4,6-tBu_3-PhOH; BDE = 82 kcal/mol). The major species in the maroon and green spectra corresponds to **2**. The major species in the blue spectrum corresponds to **3**.

---

^{31}P NMR and GC/MS analyses suggest that **7** is capable of transferring an oxygen atom to trimethylphoshine (PMe_3), where the other Fe^{III}-oxo clusters display no reaction towards the phosphine on a similar timescale (Figure 11). The difference in reactivity is likely due to

the low reduction potentials of **5** and **6** precluding efficient oxygen atom transfer reactivity. A more oxidizing cluster, through oxidations of the distal Fe centers, **7** can undergo OAT.

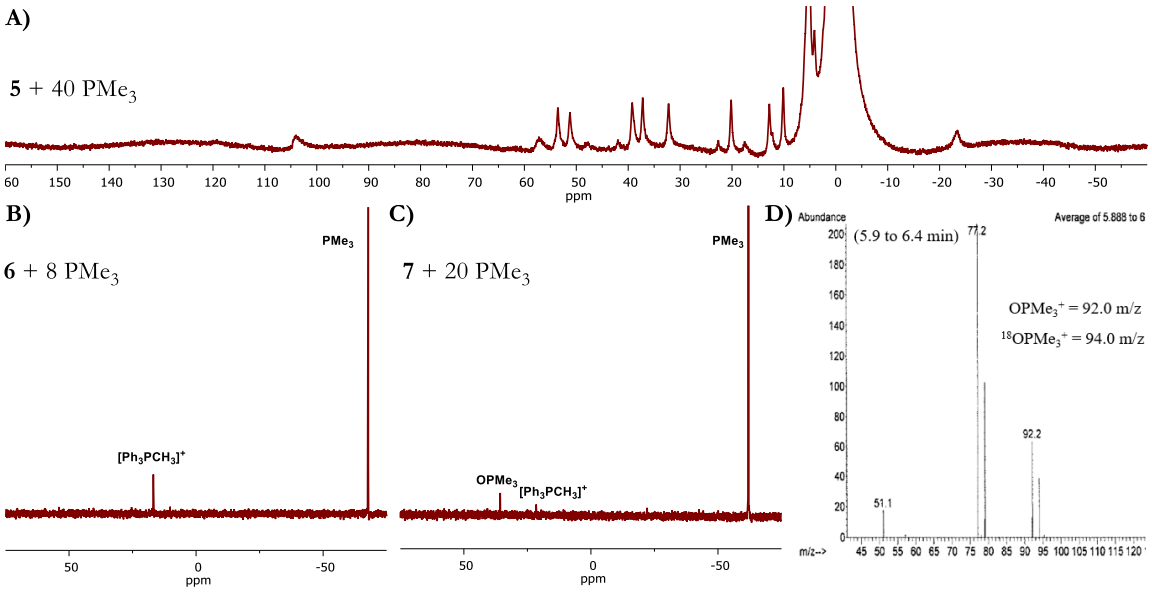

Figure 11. (A) ^{1}H NMR spectrum (400 MHz) in THF/C_6D_6 of **5** with 40 equivalents trimethylphosphine (PMe_3); the resonances are consistent with no reaction occurring. (B) ^{31}P NMR spectrum of **6** and 8 equivalents PMe_3; the only resonances observed on those assigned to unreacted PMe_3 and the conjugate acide of the based used to prepare **6** ($Ph_3PCH_3^+$). (C) ^{31}P NMR spectrum of **7** and 20 equivalents PMe_3, where a resonance assigned to trimethylphosphine oxide ($OPMe_3$) is observed ~ 40 ppm. (D) GC/MS analysis of reaction between **^{18}O-7** and PMe_3 contains mass fragments of $^{18}OPMe_3$ (94 m/z), consistent with oxygen atom transfer from **7** to form the phoshpine oxide.

The kinetics of C–H activation by these clusters was investigated. The reaction between **5** and 9,10-dihydroanthracene (DHA; BDE_{C-H} = 78 kcal/mol)[15c] displays an expected first order dependence on substrate concentration, with an overall second order rate constant of 87 M^{-1} s^{-1}, and a considerable kinetic isotope effect (KIE) of 7 with d_4-DHA. These data are consistent with a rate-limiting C–H bond activation for the PCET process to form **1** and anthracene. The

second-order rate constants between **5** and C–H bonds of varying $BDE_{C–H}$ and pK_a values were measured and display a linear dependence of the PCET reaction rate on the pK_a of the organic substrate (Figure 12), suggesting either a concerted or stepwise pK_a-driven process.[20] Reactions between DHA and **6** or **7** produce the corresponding hydroxide-clusters and anthracene in yields comparable to **5** (Table 6) indicating PCET processes, but complex kinetics precluded the determination of rate constants and further insights into the mechanism of these reactions.

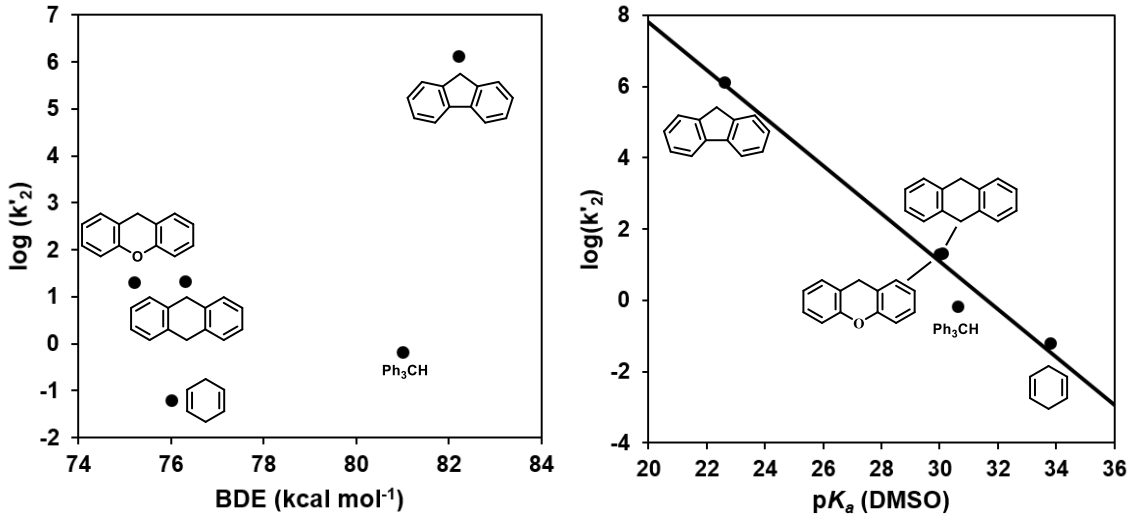

Figure 12. Plots of log (k_2) (normalized to number of reactive C-H bonds) versus BDE (left) and pK_a (in DMSO; right) for **5** with various organic substrates.

Table 6. Product Analysis of PCET and OAT Reactivity of 5 – 7.

	5		**6**		**7**	
Substrate	organic product	cluster product	organic product	cluster product	organic product	cluster product
9,10 -dihydroanthracene	anthracene (53%)[a]	**1** (67%)[b]	anthracene (43%)[a]	**2** (66%)[b]	anthracene (44%)[a]	**3** (110%)[b]
fluorene	n.d.[c]	**1** (83%)[b]	9,9'-bifluorenyl (1%)[a]	**2** (81%)	n.d.[c]	**3** (107%)[b]
2,4,6-tri-tertbutylphenol	-	**2**	phenoxyl radical[d]	**2**	-	**3**
trimethylphosphine	N.R.[e]	N.R.[e]	N.R.[e]	N.R.[e]	$OPMe_3$	**2**

[a]Quanitified by GC/MS versus authentic samples, with triphenylphosphine as an internal standard; percent yield based on a 2:1 cluster/product stoichiometry. [b]Quantified by ^{1}H NMR spectroscopy with 1,3-trimethylsilyl-benzene as an internal standard. [c]Not detected by GC/MS. [d]X-band EPR signal detected at 77 K that matches authentic sample of the corresponding phenoxyl radical.[e] No reaction observed.

CONCLUSIONS

Overall, this report offers a rare systematic study of the effects of neighboring redox active metals on structural and reactivity aspects of a terminal metal-oxo. Because it is part of a cluster, the reactivity of the terminal metal-oxo motif can be tuned without changing the formal redox state of the metal supporting it; however, redox events at distal centers have significant effect on the acidity and BDE of the corresponding O-H bond. Clearly, the cluster as an assembly is essential for reactivity beyond the structural aspects of the isolated metal-oxo motif. Further development of multinuclear model systems is necessary to fully understand the nature and amplitude of these effects.

EXPERIMENTAL DETAILS

General Considerations. All reactions were performed at room temperature in an N_2-filled M. Braun glovebox or using standard Schlenk techniques unless otherwise specified; reactions with KOH were performed in an N_2-filled VAC wetbox. Glassware was oven dried at 140 ºC for at least 2 h prior to use, and allowed to cool under vacuum. **[LFe$_3$(OAc)(OTf)][OTf]**,[11] iodosylbenzene,[21] benzyl potassium,[22] Fe(OTf)$_2$ • 2 MeCN,[23] ferrocenium trifluoromethane sulfonate ([Fc][OTf]),[24] and Ph_3PCH_2[25] were prepared according to literature procedures. *N-tert*-butyl-1*H*-pyrazol-5-amine (HPzNHtBu) was prepared according to a modified literature procedure.[26] 18-oxygen labeled potassium hydroxide ($K^{18}OH$) was prepared by quenching a tetrahydrofuran solution of benzyl potassium (less than 1 mmol) with $H_2{}^{18}O$, and drying the resulting white suspension under vacuum. Tetrahydrofuran, CH_2Cl_2, diethyl ether, benzene, toluene, acetonitrile, hexanes, and pentane were dried by sparging with nitrogen for at least 15 minutes, then passing through a column of activated A2 alumina under positive N_2 pressure. ^{1}H spectra were recorded on a Varian 300 MHz spectrometer; ^{13}C NMR spectra were recorded on a Varian 500 MHz spectrometer. ^{1}H and ^{31}P NMR spectra in THF/C_6D_6 were recorded on a Varian 500 MHz spectrometer using solvent suppression protocols. NMR spectra collected at low temperature were recorded on a Bruker 500 MHz spectrometer. CD_3CN, C_6D_6, and CD_2Cl_2 was purchased from Cambridge Isotope Laboratories, dried over calcium hydride, degassed by three freeze-pump-thaw cycles, and vacuum transferred prior to use.

Physical Methods. *Mössbauer measurements.* Zero applied field ^{57}Fe Mossbauer spectra were recorded at 80 K in constant acceleration mode on a spectrometer from See Co (Edina, MN) equipped with an SVT-400 cryostat (Janis, Wilmington, WA). The isomer shifts are relative to

the centroid of an α-Fe foil signal at room temperature. Samples were prepared by mixing polycrystalline material (20 mg) with boron nitride in a cup fitted with screw cap or freezing a concentrated acetonitrile solution in the cup. The data were fit to Lorentzian lineshapes using WMOSS (www.wmoss.org).

Mössbauer simulation details for all compounds. All spectra were simulated by four pairs of symmetric quadrupole doublets with equal populations and Lorentzian lineshapes. They were refined to a minimum via least squares optimization (13 fitting parameters per spectrum). Signals appearing above 2 mm/s were indicative with the presence of high-spin Fe^{II} centers and correspond to species with isomer shifts of ~ 1 mm/s. The Mössbauer data were fit to be consistent with our previously reported Fe clusters.[7a, 7b, 11, 27] The observed Mossbauer parameters are in agreement with related six-coordinate high-spin Fe^{II}/Fe^{III} centers.[28]

Electrochemical measurements. CVs and SWVs were recorded with a Pine Instrument Company AFCBP1 biopotentiostat with the AfterMath software package. All measurements were performed in a three electrode cell, which consisted of glassy carbon (working; ø = 3.0 mm), silver wire (counter) and bare platinum wire (reference), in a N_2 filled M. Braun glovebox at RT. Dry acetonitrile or tetrahydrofuran that contained ~100 mM $[Bu_4N][PF_6]$ was used as the electrolyte solution. The ferrocene/ferrocinium (Fc/Fc^+) redox wave was used as an internal standard for all measurements.

X-ray crystallography. X-ray diffraction data was collected at 100 K on a Bruker PHOTON100 CMOS based diffractometer (microfocus sealed X-ray tube, Mo Kα (λ) = 0.71073 Å or Cu Kα (λ) = 1.54178 Å). All manipulations, including data collection, integration, and scaling, were carried out using the Bruker APEXII software. Absorption corrections were applied using SADABS. Structures were solved by direct methods using XS (incorporated into SHELXTL) and refined by using ShelXL least squares on Olex2-1.2.7 to convergence. All

non-hydrogen atoms were refined using anisotropic displacement parameters. Hydrogen atoms were placed in idealized positions and refined using a riding model. Due to the size of the compounds (**1** – **3**, **5**, and **6**), most crystals included solvent-accessible voids that contained disordered solvent. In most cases the solvent could be modeled satisfactorily.

Magnetic measurements. Magnetic susceptibility measurements were collected on a Quantum Design DynaCool 14T PPMS instrument at the University of Southern California, Los Angeles. Polycrystalline samples (10 – 20 mg) of **2** – **4** were packed in VSM sample holders. Magnetization data at 100 K from 0 to 4 T were collected to confirm the absence of ferromagnetic impurities. Magnetic susceptibility measurements were collected between 2 and 300 K with a 0.1 T field. Reduced magnetization data was collected between 2 K and 8 K at fields between 1 T and 12 T. Magnetic data was simulated with PHI.[29]

Synthetic Procedures. *Synthesis of 2-tert-butyl-isoxazolium tetrafluoroborate.* 25 mL isoxazole (0.4 mol) was combined with 37 mL *tert*-butanol (0.4 mol) in a 500 mL roundbottom flask. This was cooled to -20 °C with an ice/sodium chloride bath while 160 mL tetrafluoroboric acid diethyl ether complex (1.2 mol) was added dropwise over 1 hour. After the addition was complete, the reaction was warmed to room temperature and stirred for 4 hours. Then, 100 mL Et_2O and 50 mL THF was added to the reaction and cooled to -20 °C; the resulting precipitate was collected on a glass frit, washed three times with 200 mL Et_2O and dried under reduced pressure. 60 g of 2-*tert*-butyl-isoxazolium tetrafluoroborate (72% yield) can be obtained this way; another 6 g can be obtained by cooling the filtrate and Et_2O washings to -20 °C overnight and collecting the resulting crystals (79% overall yield). ^{1}H NMR (300 MHz, $(CD_3)_2CO$): δ 1.90 (s, 9H), 7.46 (s, 1H), 9.55 (s, 1H), 9.77 (s, 1H) ppm.

Synthesis of N-tert-butyl-1H-pyrazol-3-amine (HPzNHtBu). This procedure was adapted from a report describing the synthesis of *tert*-butyl substituted 3-aminopyrazoles.[26] 10.0 g of 2-*tert*-

butyl-isoxazolium tetrafluoroborate (47 mmol) was suspended in 100 mL EtOH in a 250 mL roundbottom flask and cooled with an ice bath to 0 °C. A solution of 4.56 mL hydrazine monohydrate (94 mmol) in 20 mL EtOH was added dropwise to the cooled flask. After complete addition, the reaction was warmed to room temperature and stirred for 30 minutes. EtOH was removed via rotary evaporation and an aqueous work up was performed with 100 mL H_2O and 3 x 100mL CH_2Cl_2, collecting the organic layers. The combined organic fractions were dried with Na_2SO_4, filtered, and dried to yield an orange oil. The crude product was purified via Kugelrohr distillation under dynamic vacuum at 90 °C. The distillate was recrystallized with Et_2O and the resulting white solid was sublimed under vacuum at 60 °C to yield 1.6 g of HPzNHtBu (24% yield). ^{1}H NMR (400 MHz, CD_2Cl_2): δ 1.27 (s, 9H), 3.61 (br), 5.71 (d, 1H), 7.34 (d, 1H), 9.75 (br) ppm. $^{13}C\{^1H\}$ NMR (100 MHz, CD_2Cl_2): 53.28, 75.11, 118.60, 154.26 ppm (a signal for the *tert*-butyl quaternary carbon was likely not observed). Anal. calcd. (%) for $C_7H_{13}N_3$: C, 60.40; H, 9.41; N, 30.19. Found: C, 60.75; H, 9.37; N, 30.20.

Synthesis of potassium N-tert-butyl-1H-pyrazol-3-amine-ate (KPzNHtBu). 1.25 g *N-tert*-butyl-1*H*-pyrazol-3-amine (9 mmol) was dissolved in 5 mL THF. A THF solution of 1.17 g benzyl potassium (9 mmol) was added dropwise, while stirring. After 30 minutes, the reaction was concentrated to 5 mL, and the precipitate was collected via filtration. The precipitate was washed with Et_2O and dried under vacuum to yield 1.2 g KPzNHtBu as a white solid (75% yield). Anal. calcd. (%) for $C_7H_{12}KN_3$: C, 47.42; H, 6.82; N, 23.70. Found: C, 47.50; H, 6.83; N, 23.61.

*Synthesis of $LFe_3O(PzNHtBu)_3Fe(OH)$ (**1**).* 1.287 g (0.93 mmol) $LFe_3(OAc)(OTf)_2$ was suspended in THF and froze in a liquid nitrogen cooled cold well. 502.6 mg (2.83 mmol) KPzNHtBu was added with THF while the suspension was thawing. After stirring at room temperature for 1 hour, 207.0 mg (0.94 mmol) iodosylbenzene was added with THF. After 4

hours, the solvent was removed under reduced pressure. The brown solid was transferred to a coarse porosity glass frit with celite using 50 mL pentane. The desired compound was extracted using toluene until the filtrate appeared colorless. This red-brown solution was dried completely under reduced pressure; the resulting solid (1.207 g obtained) is used in the following steps assuming a molecular formula of $LFe_3O(PzNHtBu)_3$, however this could not be confirmed via X-ray crystallography due to its poor crystallinity.

110.7 mg (0.076 mmol) of the $LFe_3O(PzNHtBu)_3$ solid was dissolved in 5 mL THF. 33.0 mg (0.076 mmol) $Fe(OTf)_2$ • 2 MeCN was added with 1 mL THF. After 45 minutes, 26 mg (0.464 mmol) KOH was added as a THF suspension. After 18 hours, the reaction appeared dark blue; this solution was transferred to a Schlenk tube and dried under vacuum at 100 °C for 1 hour. The reaction mixture is suspended in MeCN and the blue precipitate was collected over a coarse porosity frit with celite. The precipitate was washed with MeCN until the filtrate was colorless, and then dried under vacuum. The dry blue precipitate was extracted with toluene and dried under reduced pressure. This residue was recrystallized via benzene/HMDSO vapor diffusion to yield 25.7 mg (0.017 mmol; 22% yield) of **1** as a blue solid. ^{1}H NMR (300 MHz, C_6D_6): δ 123.0 (br), 64.6 (br), 56.4, 50.1, 44.1, 41.0, 24.6, 19.6, 14.2, 12.2, 4.4, 3.2, 1.7, -40.6 (br) ppm. UV-Vis (THF) [ε (M^{-1} cm^{-1})] 253 nm (5.19×10^4), 494 nm (3.26×10^3), 609 nm (3.81×10^3). Anal. calcd. (%) for $C_{78}H_{76}Fe_4N_{15}O_5$: C, 61.36; H, 5.02; N, 13.76. Found: C, 61.27; H, 5.40; N, 13.12.

The 18-O labeled cluster could be prepared through the analogous protocol, substituting $K^{18}OH$ for KOH. The resulting product has identical spectroscopic features to that of **1**, and was used to prepare the remaining 18-O labeled clusters (via oxidations and/or deprotonation). ESI-MS analysis was consistent with 18-O incorporation of the cluster (Figure S18).

*Synthesis of [LFe$_3$O(PzNHtBu)$_3$Fe(OH)][OTf] (**2**).* 265.2 mg (0.17 mmol) LFe$_3$O(PzNHtBu)$_3$Fe(OH) was dissolved in 5 mL THF. This was transferred to a stirring suspension of 52.3 mg (0.16 mmol) [Fc][OTf] in 3 mL THF. After 1 hour, the reaction was concentrated under vacuum to 1 mL and 15 mL toluene was added. The reaction was stirred for 15 minutes and the resulting red-purple precipitate was collected on a coarse frit with celite and dried completely under vacuum. The red-purple solid was extracted by washing with MeCN until the filtrate appeared colorless; this solution was dried under reduced pressure. The resulting residue was recrystallized via THF/Et$_2$O vapor diffusion to yield 211 mg of red-purple crystals of **2** (0.13 mmol; 82% yield). ^{1}H NMR (300 MHz, CD$_3$CN): δ 127.2 (br), 82.1 (br), 54.4, 49.0, 22.1, 16.5 (br), 14.1, 13.8, 13.3, 10.3 (br), 8.4, 7.8, 7.3, 1.0, -4.9, -5.1, -22.8 (br) ppm. UV-Vis (ACN) [ε (M^{-1} cm^{-1})] 243 nm (5.96 x 10^4), 328 nm (8.83 x 10^3), 503 nm (4.88 x 10^3). Anal. calcd. (%) for $C_{79}H_{76}F_3Fe_4N_{15}O_8S$: C, 56.61; H, 4.57; N, 12.54. Found: C, 56.72; H, 4.70; N, 12.03.

*Synthesis of [LFe$_3$O(PzNHtBu)$_3$Fe(OH)][OTf]$_2$ (**3**).* 102.3 mg (0.06 mmol) [LFe$_3$O(PzNHtBu)$_3$Fe(OH)][OTf] was dissolved in 3 mL DCM and a solution of 20.3 mg (0.06 mmol) [Fc][OTf] in 2 mL DCM was transferred to this stirring solution. After 2 hours, 10 mL pentane was added to the reaction and the blue precipitate was collected on a coarse porosity glass frit with celite. The blue powder was dried under vacuum and extracted with DCM until colorless, and recrystallized from DCM/Et$_2$O to obtain 76.8 mg of **3** as blue crystals (69% yield) ^{1}H NMR (300 MHz, CD_2Cl_2): δ 144.3 (br), 103.7 (br), 82.0, 79.7, 66.0, 63.1, 15.5, 12.8, 9.9, 3.5, 1.2, -0.5, -2.3 (br), -11.6 (br) ppm. [ε (M^{-1} cm^{-1})] 238 nm (5.76 x 10^4), 345 nm (7.74 x 10^3), 634 nm (4.80 x 10^3). Anal. calcd. (%) for $C_{80}H_{76}F_6Fe_4N_{15}O_{11}S_2$: C, 52.65; H, 4.20; N, 11.51. Found: C, 51.70; H, 4.37; N, 11.11.

*Synthesis of [LFe$_3$O(PzNHtBu)$_3$Fe(OH)][OTf]$_3$ (**4**).* 42.9 mg (0.024 mmol) [LFe$_3$O(PzNHtBu)$_3$Fe(OH)][OTf]$_2$ was dissolved in 2 mL DCM and 8.1 mg (0.024 mmol) [Fc][OTf] was added with 2 mL DCM. After 30 minutes, the reaction was concentrated and 10 mL Et_2O was added to produce a green precipitate. This was collected on a frit over celite and rinsed with Et_2O. The precipitate was collected with DCM and recrystallized via vapor diffusion of Et_2O to obtain 39.0 mg (0.020 mmol; 82% yield) **4** as green crystals. ^{1}H NMR (300 MHz, CD_2Cl_2): δ 95.2, 85.0, 14.5, -1.8, -44.9. -48.3 ppm. UV-Vis (ACN) [ε (M^{-1} cm^{-1})] 242 nm (7.11 x 10^4), 355 nm (8.85 x 10^3), 748 nm (7.39 x 10^3). Anal. calcd. (%) for $C_{81}H_{76}F_9Fe_4N_{15}O_{14}S_3$: C, 49.28; H, 3.88; N, 10.64. Found: C, 49.19; H, 4.09; N, 10.02.

*Synthesis of LFe$_3$O(PzNHtBu)$_3$Fe(O) (**5**).* 102.6 mg (0.06 mmol) [LFe$_3$O(PzNHtBu)$_3$Fe(OH)][OTf] was dissolved in 15mL THF and froze in a liquid nitrogen cooled cold well. 7.2 mg (0.06 mmol) KOtBu was added to the thawing solution, and the reaction was stirred at room temperature for 1 hour. The solvent was removed under reduced pressure and the crude product was recrystallized via benzene/HMDSO vapor diffusion to obtain 26.2 mg of **5** as purple crystals (0.02 mmol; 28% yield). ^{1}H NMR (300 MHz, C_6D_6): δ 105.9 (br), 58.5 (br), 55.3, 53.0, 40.9, 38.9, 33.9, 21.8, 14.4, 11.7, 2.4, 1.1, -21.5 (br) ppm. UV-Vis (THF) [ε (M^{-1} cm^{-1})] 248 nm (4.40 x 10^4), 342 nm (6.73 x 10^3), 539 nm (3.41 x 10^3). Anal. calcd. (%) for $C_{78}H_{75}Fe_4N_{15}O_5$: C, 61.40; H, 4.95; N, 13.77. Found: C, 60.04; H, 5.01; N, 13.06 (Calcd. (%) for $C_{78}H_{75}Fe_4N_{15}O_5$ • 0.5 ($C_6H_{18}OSi_2$): C, 60.05; H, 5.27; N, 13.08; compound recrystallized from benzene/HMDSO).

*Synthesis of [LFe$_3$O(PzNHtBu)$_3$Fe(O)][OTf] (**6**).* 50.3 mg (0.03 mmol) [LFe$_3$O(PzNHtBu)$_3$Fe(OH)][OTf]$_2$ was dissolved in 2 mL THF/DCM (1:1) and froze in a liquid nitrogen cooled cold well. 8 mg (0.03 mmol) Ph_3PCH_2 was added to the thawing solution as a THF solution. The reaction turned a deep blue, and at this point care was taken to avoid

warming the mixture to room temperature. The compound was precipitated by addition of cold Et_2O, and the precipitate was dried under vacuum to yield **6** as a blue powder. NMR analysis of this powder revealed the presence of residual $[Ph_3PCH_3][OTf]$, which were difficult to remove with Et_2O washes. This mixture could be recrystallized in THF/Et_2O at -35 °C to obtain X-ray quality crystals of **6**; however, due to the decomposition of this compound, obtaining **6** cleanly as a bulk solid for elemental analysis was unsuccessful. ^{1}H NMR (300 MHz, CD_3CN): δ 122.2 (br), 90.2 (br), 68.5, 66.1, 55.0, 53.2, 14.5, 13.9, 13.0, 10.7, -31.0 (br) ppm.

*Synthesis of [LFe$_3$O(PzNHtBu)$_3$Fe(O)][OTf]$_2$ (**7**).* 43.0 mg $[LFe_3O(PzNHtBu)_3Fe(OH)][OTf]_2$ (**3**; 0.02 mmol) was dissolved in 1:1 DCM/THF and froze in a liquid nitrogen cooled cold well. A THF solution of 6.8 mg Ph_3PCH_2 (0.02 mmol) was added to the thawing solution. The reaction was then combined, while thawing, with a DCM solution of 7.8 mg [Fc][OTf] (0.02 mmol). Keeping this mixture as cold as possible, thawing Et_2O was added to precipitate the oxidized cluster; The blue-green solid was collected on a fine porosity glass frit, and dried under vacuum. The ^{1}H NMR of this solid always contained minor amounts of impurities (<20%, mostly ascribed to **3** and **4**), which **7** could not be isolated from due to its thermal instability. For any subsequent reactions performed on this material, the moles of initial cluster **3** were used to approximate the amount of **7** present. ^{1}H NMR (300 MHz, 1:1 CD_3CN/CD_2Cl_2): δ 145.6 (br), 105.4 (br), 85.2, 81.4, 71.0, 67.2, 19.0, 13.8, 11.1, 8.8, -61.1, -67.3 (br).

Experimental Protocols. *Reactions for product analysis.* 2mM solutions of Fe-oxo clusters **5** – **7** were stirred for 12-24 hours with one equivalent of 9,10-dihydroanthracene (DHA) or fluorene. The solvent was removed under vacuum and the organic products were extracted with Et_2O containing triphenylphosphine as an internal standard. The suspensions were filtered over celite and analyzed via GC-MS. The oxidized products (anthracene and 9,9'-

bifluorene) were quantified based on a calibration curve of authentic samples. Other possible oxidation products, such as fluorenone, or anthraquinone, were not observed.

Oxygen atom transfer studies with ***^{18}O-7*** *and* PMe_3. **^{18}O-7** cluster was prepared in situ by combining a thawing 1:1 THF/DCM solution of 50.3 mg **^{18}O-3** (0.03 mmol) with 7.5 mg Ph_3PCH_2 (0.03 mmol) to prepare a solution of **6-^{18}O**. This solution was combined, while thawing, to a DCM solution of 9.5 mg [Fc][OTf] (0.03 mmol). Keeping this mixture as cold as possible, thawing Et_2O was added to precipitate the oxidized cluster; boron nitride (BN) was added to ease separation of precipitate from the solution. This suspension was filtered to obtain solid **^{18}O-7**, which was eluted from BN with cold 1:1 THF/DCM. 50 μL PMe_3 (0.50 mmol) was added to solution as it thawed, and was gradually warmed to room temperature. ^{31}P NMR analysis of the reaction mixture at this stage showed a peak consistent with trimethylphosphine oxide ($OPMe_3$) formation at ~35 ppm. After 30 minutes, the reaction was pumped down. On the bench, the crude reaction mixture was separated via silica plug; 10% MeOH in DCM was used to elute a dark solution, at which point MeOH was washed through the plug to collect a fraction containing $OPMe_3$. The MeOH fraction was pumped down and analyzed via GC/MS, which displayed a GC peak characteristic of $OPMe_3$, with both $^{16}OPMe_3$ and $^{18}OPMe_3$ based on its mass spectrum.

ELECTROCHEMICAL DETAILS

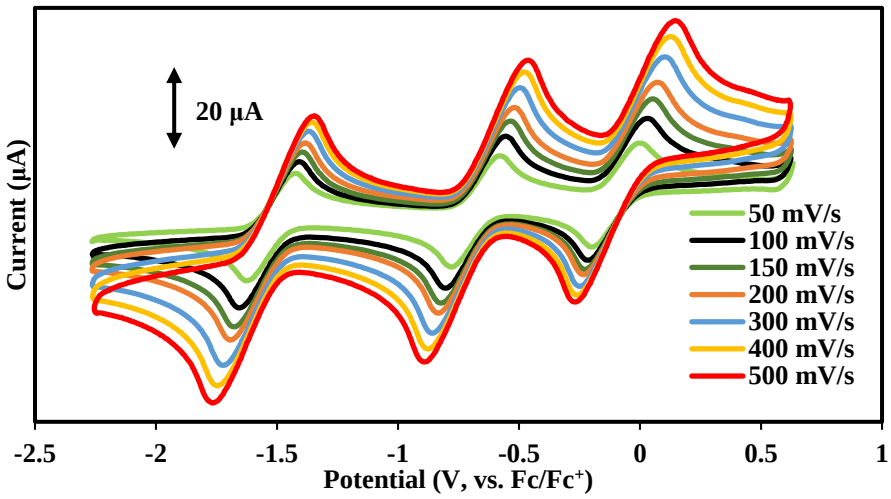

Figure 13. Cyclic voltammetry of $[LFe_3O(PzNHtBu)_3Fe(OH)][OTf]$, **2**, (2.5 mM) in THF with a glassy carbon working, platinum counter, and silver wire reference electrodes and ca. 200 mM $[Bu_4N][PF_6]$ at various scan rates.

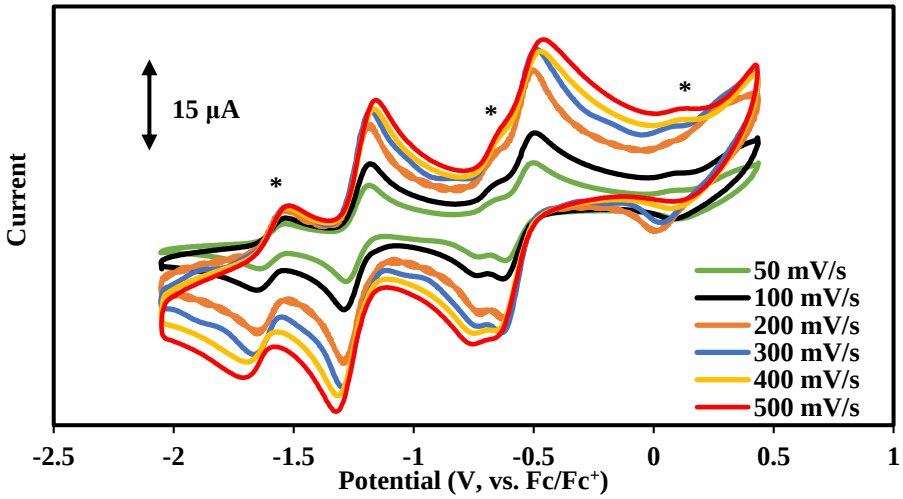

Figure 14. Cyclic voltammetry of $LFe_3O(PzNHtBu)_3Fe(O)$, **5**, (2.3 mM) in THF with a glassy carbon working, platinum counter, and silver wire reference electrodes and ca. 100 mM $[Bu_4N][PF_6]$ at various scan rates. Electrochemical events marked with an asterisk (*) are assigned to a small amount of $[LFe_3O(PzNHtBu)_3Fe(OH)]^{n+}$ that formed due to decomposition.

KINETICS DETAILS

Substrate	BDE (kcal/mol)[30]	pK_a (DMSO)	k_2 (M^{-1} s^{-1}) with **5**
xanthene	75.2	30.0[31]	40
1,4-cyclohexadiene	76.0	~34[a]	~0.3
9,10-dihydroanthracene	76.3	30.1[31]	87
triphenylmethane	81.0	30.6[32]	~0.7
fluorene	82.2	22.6[32]	~3 x 10^6

Reported bond dissociation enthalpies (in kcal mol^{-1}) and pK_a values (in DMSO) of various organic substrates investigated for PCET reactivity with $LFe_3O(PzNHtBu)_3Fe(O)$ (**5**), with their measured second order rate constants. ^{1}H NMR analysis of the reaction mixtures after kinetics measurements show formation of **1** in all cases, consistent with a PCET process.

[a]A reported pK_a value for 1,4-cyclohexadiene could not be obtained, but is approximated based on the reported pK_a value of 1,3-cyclohexadiene in DMSO (pK_a(1,3) = 35.0) and the energy of isomerization between 1,3-cyclohexadiene and 1,4-cyclohexadiene (-1.6 kcal/mol):[33]

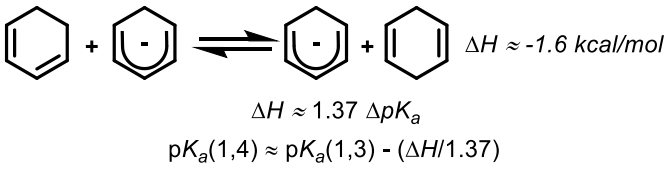

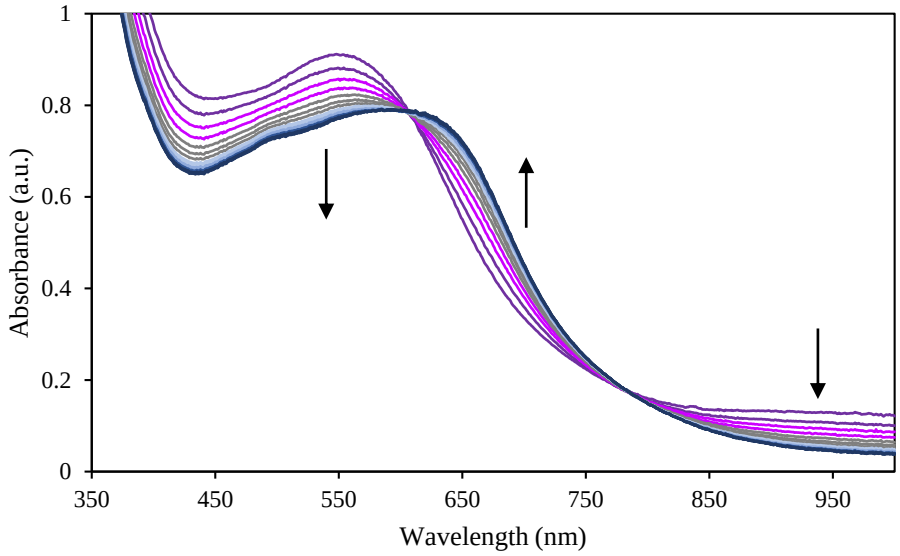

Figure 15. UV-Vis absorbance spectra of $LFe_3O(PzNHtBu)_3Fe(O)$ (**5**; 200 μM) and xanthene (10 mM) at ambient temperature.

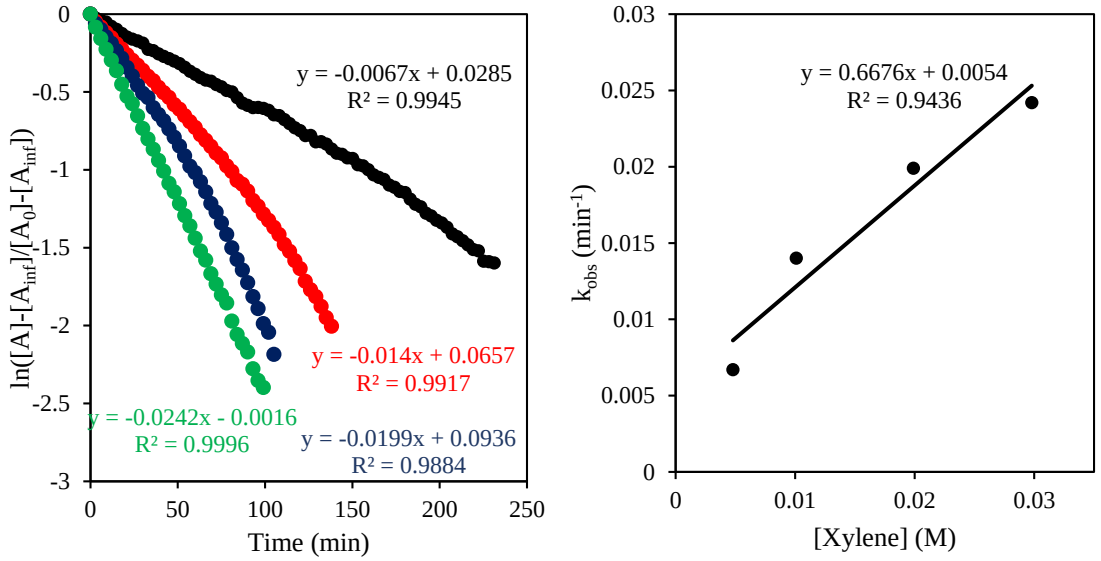

Figure 16. Kinetics data for the reaction between $LFe_3O(PzNHtBu)_3Fe(O)$ (**5**; 200 μM) and xanthene (4.8, 10.1, 19.9, and 29.8 mM) at ambient temperature. The decay of the UV-Vis absorbance feature at 540 nm was used to follow the reaction.

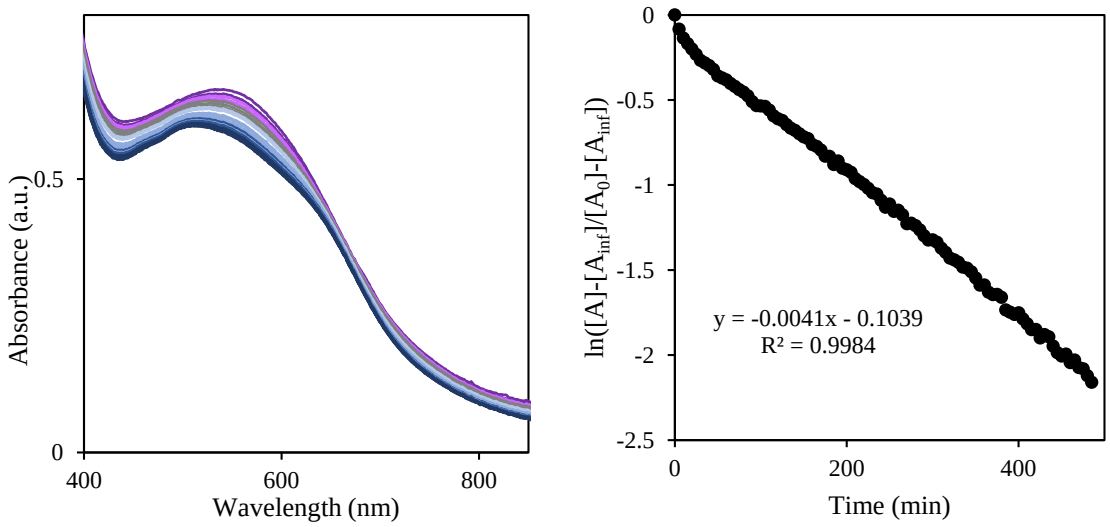

Figure 17. (Left) UV-Vis absorbance spectra of $LFe_3O(PzNHtBu)_3Fe(O)$ (**5**; 200 μM) and 1,4-cyclohexadiene (1 M) at ambient temperature. (Right) Pseudo-first order kinetics plot of the reaction by following the decay of the signal at 516 nm; this wavelength was used since the background decomposition of the compound did not affect this wavelength.

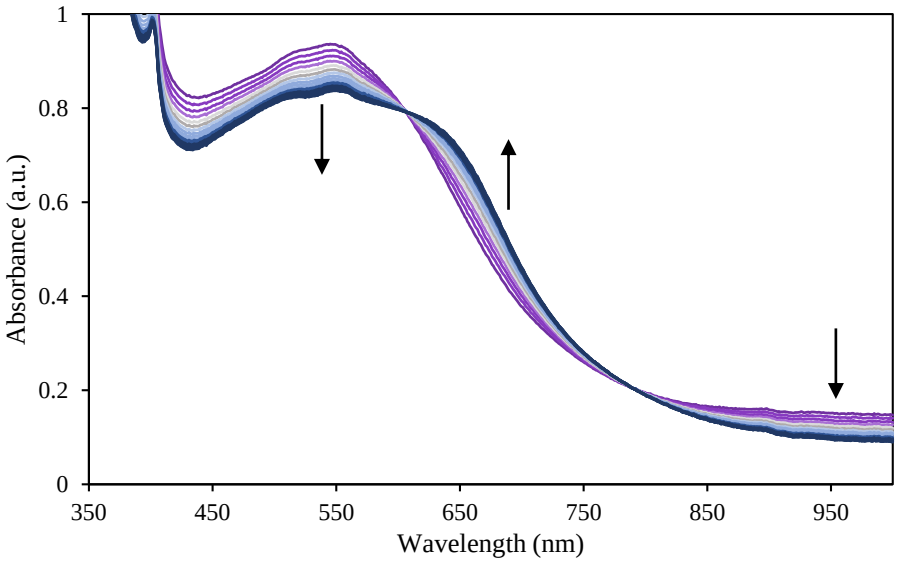

Figure 18. UV-Vis absorbance spectra of $LFe_3O(PzNHtBu)_3Fe(O)$ (**5**; 200 μM) and 9,10-dihydroanthracene (10 mM) at ambient temperature.

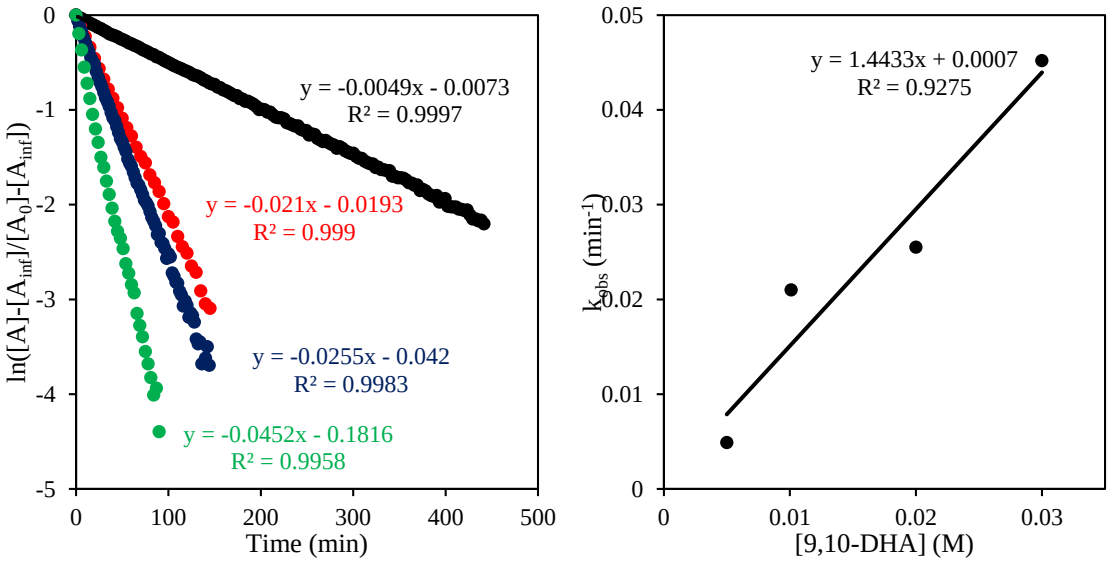

Figure 19. Kinetics data for the reaction between $LFe_3O(PzNHtBu)_3Fe(O)$ (**5**; 200 μM) and 9,10-dihydroanthracene (9,10-DHA; 5, 10, 20, and 30 mM) at ambient temperature. The decay of the UV-Vis absorbance feature at 540 nm was used to follow the reaction.

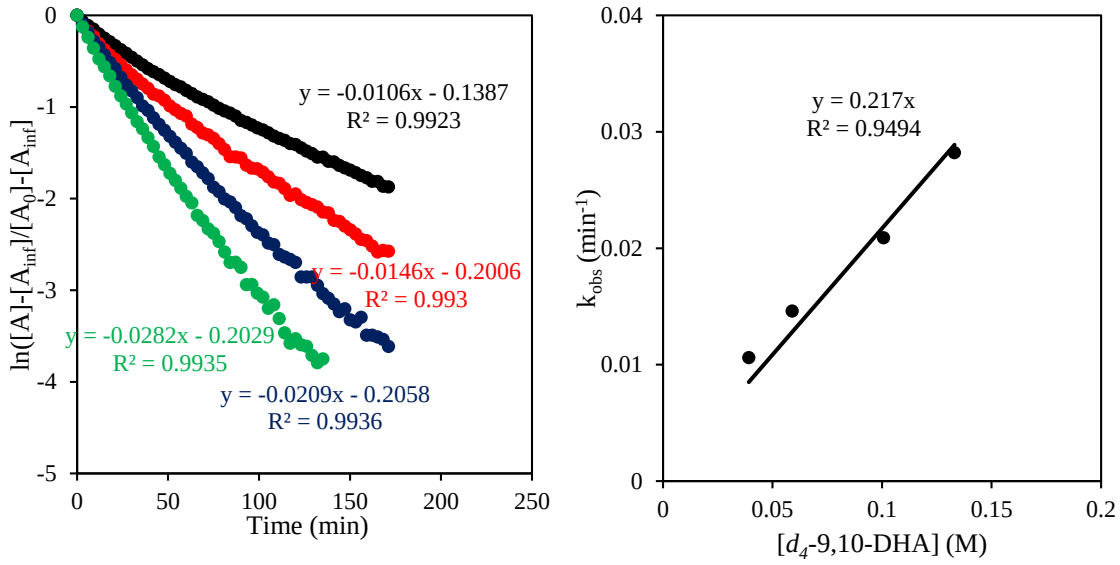

Figure 20. Kinetics data for the reaction between $LFe_3O(PzNHtBu)_3Fe(O)$ (**5**; 200 μM) and *d*$_4$-9,10-dihydroanthracene (*d*$_4$-9,10-DHA; 40, 60, 100, and 130 mM) at ambient temperature. The decay of the UV-Vis absorbance feature at 540 nm was used to follow the reaction.

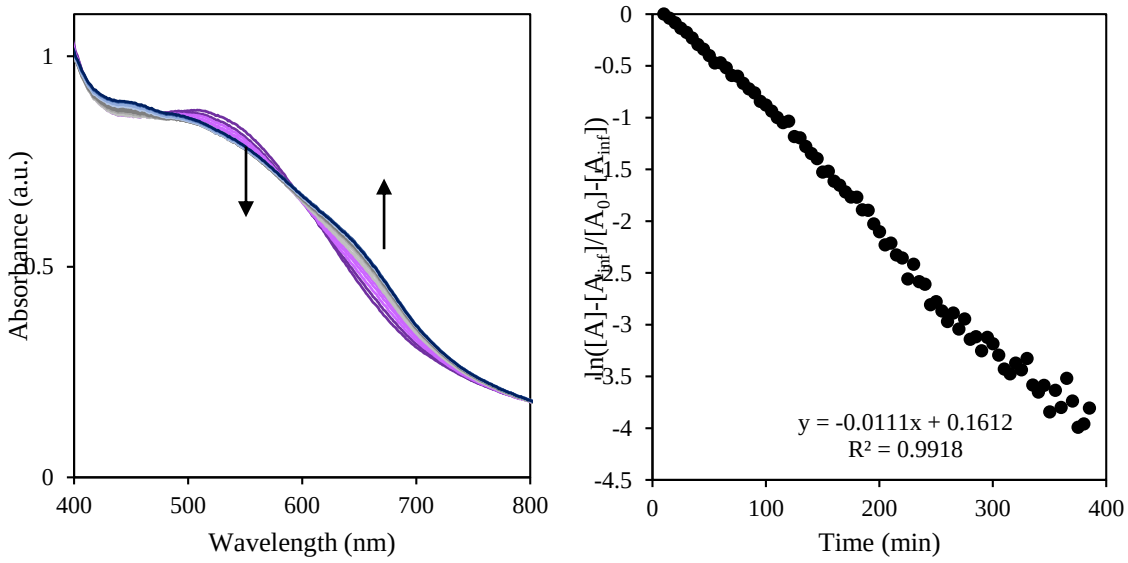

Figure 21. (Left) UV-Vis absorbance spectra of $LFe_3O(PzNHtBu)_3Fe(O)$ (**5**; 200 μM) and triphenylmethane (1 M) at ambient temperature. (Right) Pseudo-first order kinetics plot of the reaction by following the decay of the signal at 516 nm; this wavelength was used since the background decomposition of the compound did not affect this wavelength.

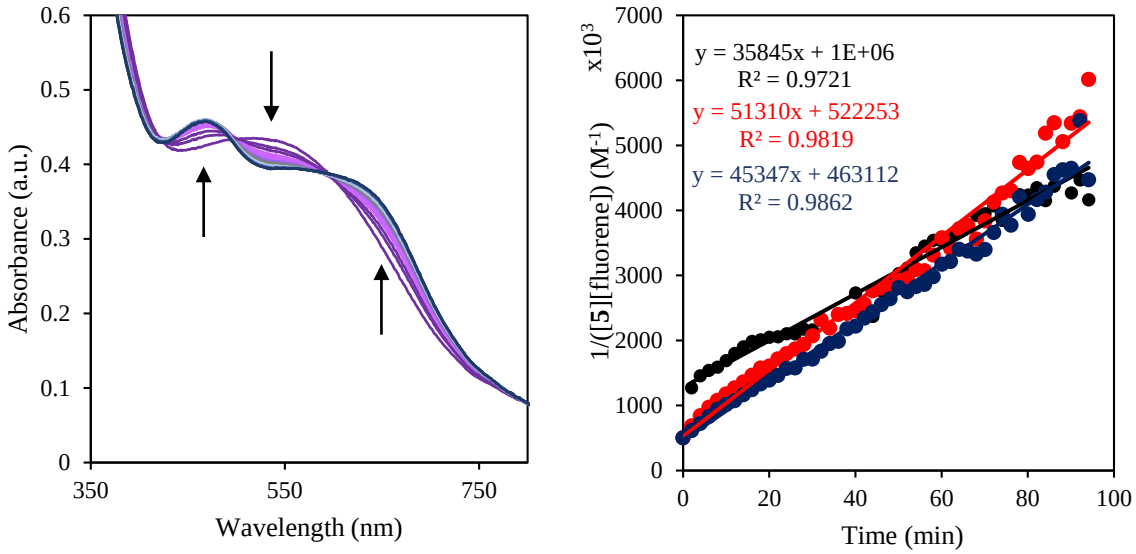

Figure 22. (Left) UV-Vis absorbance spectra of $LFe_3O(PzNHtBu)_3Fe(O)$ (**5**; 1 mM) and fluorene (2 mM) at ambient temperature in a 1 mm cuvette. (Right) Second order kinetics plot of the reaction by following the growth of the signal at 645 nm.

CRYSTALOGRAPHIC DETAILS

Crystal and refinement data for complexes 1 – 3, 5, and 6.

	1	**2-PF_6**	**3**	**5**	**6**
CCDC Number	1903350	1903348	1903352	1903351	1903349
Empirical formula	$C_{90}H_{88}Fe_4N_{15}O_5$	$C_{83}H_{76}F_6Fe_4N_{15}O_{5.5}P$	$C_{80}H_{76}F_6Fe_4N_{15}O_{11}S_2$	$C_{90}H_{87}Fe_4N_{15}O_5$	$C_{91}H_{99}F_3Fe_4N_{15}O_{11}S$
Formula weight (g/mol)	1683.15	1793.95	1825.07	1682.14	1673.00
Radiation	MoKα (λ = 0.71073)	CuKα (λ = 1.54178)	CuKα (λ = 1.54178)	CuKα (λ=1.54178)	CuKα (λ=1.54178)
a (Å)	14.1115(11)	11.9919(11)	12.150(2)	12.3162(13)	19.122(9)
b (Å)	15.0509(11)	13.7630(9)	14.975(5)	15.5743(15)	18.204(5)
c (Å)	21.1556(16)	25.905(2)	23.386(6)	21.6599(15)	24.698(6)
α (°)	70.794(3)	89.286(4)	95.271(14)	102.390(6)	90
β (°)	86.911(3)	87.757(4)	90.124(12)	94.445(4)	90
γ (°)	70.570(3)	79.589(4)	104.172(19)	102.897(9)	90
V (Å^3)	3993.7(5)	4201.8(6)	4106.5(18)	3921.5(7)	8597(5)
Z	2	2	2	2	4
Cryst. syst.	triclinic	triclinic	triclinic	triclinic	orthorhombic
Space group	P-1	P-1	P-1	P-1	$Pna2_1$
ϱ_{calc}g (cm^3)	1.400	1.375	1.476	1.425	1.463
2 Θ range (°)	4.74 to 77.068	6.53 to 149.628	3.796 to 148.742	6.454 to 160.188	6.032 to 130.72
μ (mm^{-1})	0.777	6.219	6.726	6.338	6.172
GOF	1.019	1.044	1.063	1.012	1.064
R1, wR2 (I>2σ (I))	0.0412, 0.0980	0.0710, 0.1919	0.0375, 0.0940	0.0400, 0.0954	0.0732, 0.1352

Special refinement details for [$LFe_3O(PzNHtBu)_3Fe(OH)][PF_6]$. A *tert*-butyl group of one of the pyrazolate ligands is partially disordered over two positions with occupancies of 39% (C93 and C94) and 61% (C97 and C98). There is significant solvent disorder that could not be fully refined, however electron density for a tetrahydrofuran (O100 and C100-C103), and two partial diethyl ether molecules (refined as C104-C109) were refined isotropically with only partial occupancy.

Special refinement details for [$LFe_3O(PzNHtBu)_3Fe(OH)][OTf]_2$. One of the outersphere triflates was modeled as disordered over two nearly identical positions, with occupancies of 75% (S101 through C101) and 25% (S102 through C102). A 'SAME' constraint was used to favor distances and angles of these disordered triflates to the non-disordered one. A partially occupied solvent molecule (likely Et_2O) was present; however, due to its position near a symmetry element, its residual electron density was removed via a solvent mask, as opposed to modeling this disordered solvent.

Special refinement details for [$LFe_3O(PzNHtBu)_3Fe(O)]$. A benzene solvent is positionally disordered over two positions with occupancies of 29% (C106-C111) and 71% (C206-C211).

Special refinement details for [$LFe_3O(PzNHtBu)_3Fe(O)][OTf]$. Generally, these crystals were of relatively poor quality compared to the other structures obtained; the crystal was twinned with a 13% twinned crystal component. While no disorder had to be modeled in the molecule, the outerphere triflate, or the three additional molecules of THF, the low intensity of high angle diffraction data led to low C–C bond precision. Initially, some carbon atoms in the ligand backbone had highly skewed ellipsoids, which were addressed with SIMU/DELU restraints (on O11, C11, C12, C26, C27, and C42 – C45) or, in one case, an ISOR restraint (C44).

Selected bond parameters for structurally characterized compounds 1-3, 5, and 6.

Bond Distance (Å)	1	2-PF_6	3	5	6
Fe1–O1	2.102(1)	2.142(3)	2.148(1)	2.139(1)	2.154(7)
Fe2–O1	2.109(1)	2.101(3)	2.002(2)	2.050(2)	1.927(7)
Fe3–O1	2.089(1)	1.952(3)	1.971(1)	1.967(2)	1.948(7)
Fe4–O1	1.837(1)	1.890(3)	1.948(2)	1.965(2)	2.049(7)
Fe4–O2	1.937(1)	1.907(3)	1.879(2)	1.817(2)	1.795(8)
Fe1–N13	2.129(1)	2.107(4)	2.074(2)	2.124(2)	2.091(9)
Fe2–N23	2.126(1)	2.106(3)	2.057(2)	2.084(2)	2.039(9)
Fe3–N33	2.120(1)	2.071(4)	2.017(2)	2.090(2)	2.015(8)
Fe4–N14	2.097(1)	2.091(4)	2.083(2)	2.093(2)	2.085(9)
Fe4–N24	2.168(1)	2.056(4)	2.047(2)	2.104(2)	2.087(9)
Fe4–N34	2.111(1)	2.105(4)	2.059(2)	2.098(2)	2.100(8)
N13–N14	1.382(1)	1.373(5)	1.377(2)	1.388(2)	1.396(12)
N23–N24	1.368(1)	1.387(5)	1.394(2)	1.387(3)	1.384(11)
N33–N34	1.386(1)	1.389(5)	1.397(2)	1.378(3)	1.387(12)
N15–C72	1.397(2)	1.417(7)	1.422(3)	1.400(3)	1.379(14)
N25–C82	1.422(2)	1.354(7)	1.356(3)	1.366(5)	1.391(14)
(N26–C82)	-	-	-	1.41(2)	-
N35–C92	1.393(2)	1.383(7)	1.350(3)	1.402(3)	1.341(14)
Bond Angles (º)					
N14–Fe4–N24	120.1	119.1	116.6	118.3	113.4
N24–Fe4–N34	122.1	118.8	119.8	123.0	119.6
N34–Fe4–N14	117.8	121.7	122.7	117.5	124.0
N14–Fe4–O2	88.4	91.7	92.6	96.3	97.6
N24–Fe4–O2	91.3	93.5	95.0	92.0	96.3
N34–Fe4–O2	92.2	91.1	92.1	92.8	93.6
O1–Fe4–O2	177.1	177.3	178.7	177.1	176.0
Torsion Angles (º)					
Fe1–N13–N14–Fe4	13.9	2.7	6.2	19.4	21.9
Fe2–N23–N24–Fe4	11.6	9.9	8.2	4.5	17.4
Fe3–N33–N34–Fe4	13.4	12.5	11.1	13.7	2.7
Centroid Distances (Å)					
Fe1|Fe2|Fe3–N14|N24|N34	2.050	1.701	1.643	1.685	1.627
Fe1|Fe2|Fe3–O11|O21|O31	1.121	1.110	1.078	1.120	1.122
Fe1|Fe2|Fe3–O1	1.153	1.105	1.036	1.076	1.012
N14|N24|N34–Fe4	0.025	0.075	0.120	0.138	0.218

References

1. (a) Que Jr, L.; Tolman, W. B. *Nature* **2008,** *455*, 333; (b) Hohenberger, J.; Ray, K.; Meyer, K. *Nature Communications* **2012,** *3*, 720; (c) Costas, M.; Mehn, M. P.; Jensen, M. P.; Que, L. *Chem. Rev.* **2004,** *104*, 939-986; (d) Blakemore, J. D.; Crabtree, R. H.; Brudvig, G. W. *Chem. Rev.* **2015,** *115*, 12974-13005; (e) Nguyen, A. I.; Ziegler, M. S.; Oña-Burgos, P.; Sturzbecher-Hohne, M.; Kim, W.; Bellone, D. E.; Tilley, T. D. *J. Am. Chem. Soc.* **2015,** *137*, 12865-12872; (f) Okamura, M.; Kondo, M.; Kuga, R.; Kurashige, Y.; Yanai, T.; Hayami, S.; Praneeth, V. K. K.; Yoshida, M.; Yoneda, K.; Kawata, S.; Masaoka, S. *Nature* **2016,** *530*, 465-468; (g) Hunter, B. M.; Thompson, N. B.; Müller, A. M.; Rossman, G. R.; Hill, M. G.; Winkler, J. R.; Gray, H. B. *Joule* **2018,** *2*, 747-763.
2. Yano, J.; Yachandra, V. *Chem. Rev.* **2014,** *114*, 4175-4205.
3. (a) Ichino, T.; Yoshioka, Y. *Chem. Phys. Lett.* **2014,** *595–596*, 237-241; (b) Yamaguchi, K.; Isobe, H.; Yamanaka, S.; Saito, T.; Kanda, K.; Shoji, M.; Umena, Y.; Kawakami, K.; Shen, J. R.; Kamiya, N.; Okumura, M. *Int. J. Quantum Chem* **2013,** *113*, 525-541; (c) Sproviero, E. M.; Gascón, J. A.; McEvoy, J. P.; Brudvig, G. W.; Batista, V. S. *J. Am. Chem. Soc.* **2008,** *130*, 3428-3442; (d) Siegbahn, P. E. M. *BBA - Bioenergetics* **2013,** *1827*, 1003-1019.
4. Limburg, J.; Vrettos, J. S.; Liable-Sands, L. M.; Rheingold, A. L.; Crabtree, R. H.; Brudvig, G. W. *Science* **1999,** *283*, 1524-1527.
5. (a) Ozaki, S.-i.; Roach, M. P.; Matsui, T.; Watanabe, Y. *Acc. Chem. Res.* **2001,** *34*, 818-825; (b) Betley, T. A.; Wu, Q.; Van Voorhis, T.; Nocera, D. G. *Inorg. Chem.* **2008,** *47*, 1849-1861; (c) Guo, M.; Corona, T.; Ray, K.; Nam, W. *ACS Cent Sci* **2019,** *5*, 13-28; (d) Sacramento, J. J. D.; Goldberg, D. P. *Acc. Chem. Res.* **2018,** *51*, 2641-2652; (e) Goetz, M. K.; Hill, E. A.; Filatov, A. S.; Anderson, J. S. *J. Am. Chem. Soc.* **2018,** *140*, 13176-13180; (f) Usharani, D.; Janardanan, D.; Li, C.; Shaik, S. *Acc. Chem. Res.* **2013,** *46*, 471-482; (g) Kim, S. H.; Park, H.; Seo, M. S.; Kubo, M.; Ogura, T.; Klajn, J.; Gryko, D. T.; Valentine, J. S.; Nam, W. *J. Am. Chem. Soc.* **2010,** *132*, 14030-14032; (h) Kurahashi, T.; Kikuchi, A.; Shiro, Y.; Hada, M.; Fujii, H. *Inorg. Chem.* **2010,** *49*, 6664-6672; (i) Gunay, A.; Theopold, K. H. *Chem. Rev.* **2010,** *110*, 1060-1081.
6. (a) de Visser, S. P.; Kumar, D.; Neumann, R.; Shaik, S. *Angew. Chem. Int. Ed.* **2004,** *43*, 5661-5665; (b) Khenkin, A. M.; Kumar, D.; Shaik, S.; Neumann, R. *J. Am. Chem. Soc.* **2006,** *128*, 15451-15460; (c) Xue, G.; De Hont, R.; Münck, E.; Que, L., Jr. *Nature Chemistry* **2010,** *2*, 400-405; (d) Vaddypally, S.; Kondaveeti, S. K.; Karki, S.; Van Vliet, M. M.; Levis, R. J.; Zdilla, M. J. *J. Am. Chem. Soc.* **2017,** *139*, 4675-4681; (e) Sarma, R.; Angeles-Boza, A. M.; Brinkley, D. W.; Roth, J. P. *J. Am. Chem. Soc.* **2012,** *134*, 15371-15386.
7. (a) de Ruiter, G.; Thompson, N. B.; Takase, M. K.; Agapie, T. *J. Am. Chem. Soc.* **2016,** *138*, 1486-1489; (b) de Ruiter, G.; Carsch, K. M.; Gul, S.; Chatterjee, R.; Thompson, N. B.; Takase, M. K.; Yano, J.; Agapie, T. *Angew. Chem. Int. Ed.* **2017,** *56*, 4772-4776; (c) Carsch, K. M.; de Ruiter, G.; Agapie, T. *Inorg. Chem.* **2017,** *56*, 9044-9054.
8. (a) Lacy, D. C.; Gupta, R.; Stone, K. L.; Greaves, J.; Ziller, J. W.; Hendrich, M. P.; Borovik, A. S. *J. Am. Chem. Soc.* **2010,** *132*, 12188-12190; (b) Gupta, R.; Taguchi, T.; Lassalle-Kaiser, B.; Bominaar, E. L.; Yano, J.; Hendrich, M. P.; Borovik, A. S. *Proc. Natl. Acad. Sci.* **2015,** *112*, 5319-5324; (c) Gupta, R.; MacBeth, C. E.; Young, V. G.; Borovik, A. S. *J. Am. Chem. Soc.* **2002,** *124*, 1136-1137; (d) Gupta, R.; Borovik, A. S. *J. Am. Chem. Soc.* **2003,** *125*, 13234-13242; (e) MacBeth, C. E.; Golombek, A. P.; Young, V. G.; Yang, C.; Kuczera, K.; Hendrich, M. P.; Borovik, A. S. *Science* **2000,** *289*, 938-941; (f) Ford, C. L.; Park, Y. J.; Matson, E. M.; Gordon, Z.; Fout, A. R. *Science* **2016,** *354*, 741; (g) Park, Y. J.; Matson, E. M.; Nilges, M. J.; Fout, A. R. *Chem. Commun.* **2015,** *51*, 5310-5313; (h) Matson, E. M.; Park, Y. J.; Fout, A. R. *J. Am. Chem. Soc.* **2014,** *136*, 17398-17401; (i) Gordon, Z.; Drummond, M. J.; Matson, E. M.; Bogart, J. A.; Schelter, E. J.; Lord, R. L.; Fout, A. R. *Inorg. Chem.* **2017,** *56*, 4852-4863.
9. Han, Z.; Horak, K. T.; Lee, H. B.; Agapie, T. *J. Am. Chem. Soc.* **2017,** *139*, 9108-9111.
10. Horak, K. T. The Design and Synthesis of Transition Metal Complexes Supported by Non-innocent Ligand Scaffolds for Small Molecule Activation. PhD dissertation, California Institute of Technology, Pasadena, California, 2016.
11. de Ruiter, G.; Thompson, N. B.; Lionetti, D.; Agapie, T. *J. Am. Chem. Soc.* **2015,** *137*, 14094-14106.

12. Arnett, C. H.; Chalkley, M. J.; Agapie, T. *J. Am. Chem. Soc.* **2018,** *140*, 5569-5578.
13. Andris, E.; Navrátil, R.; Jašík, J.; Puri, M.; Costas, M.; Que, L.; Roithová, J. *J. Am. Chem. Soc.* **2018,** *140*, 14391-14400.
14. McDonald, A. R.; Que Jr, L. *Coord. Chem. Rev.* **2013,** *257*, 414-428.
15. (a) Bordwell, F. G.; Satish, A. V.; Zhang, S.; Zhang, X. M. Using thermodynamic cycles to study reactive intermediates. In *Pure Appl. Chem.*, 1995; Vol. 67, p 735; (b) Mayer, J. M. *Acc. Chem. Res.* **1998,** *31*, 441-450; (c) Warren, J. J.; Tronic, T. A.; Mayer, J. M. *Chem. Rev.* **2010,** *110*, 6961-7001.
16. (a) Saame, J.; Rodima, T.; Tshepelevitsh, S.; Kütt, A.; Kaljurand, I.; Haljasorg, T.; Koppel, I. A.; Leito, I. *The Journal of Organic Chemistry* **2016,** *81*, 7349-7361; (b) Garrido, G.; Koort, E.; Ràfols, C.; Bosch, E.; Rodima, T.; Leito, I.; Rosés, M. *The Journal of Organic Chemistry* **2006,** *71*, 9062-9067.
17. Reed, C. J.; Agapie, T. *J. Am. Chem. Soc.* **2018,** *140*, 10900-10908.
18. PCET is broadly referred to here as the transfer of a proton and an electron to different parts of a complex (see ref. 17); the precise mechanism, whether concerted (CPET or EPT) or stepwise (either PTET or ETPT), is left ambiguous, as the present experiments cannot differentiate them.
19. Weinberg, D. R.; Gagliardi, C. J.; Hull, J. F.; Murphy, C. F.; Kent, C. A.; Westlake, B. C.; Paul, A.; Ess, D. H.; McCafferty, D. G.; Meyer, T. J. *Chem. Rev.* **2012,** *112*, 4016-4093.
20. Goetz, M. K.; Anderson, J. S. *J. Am. Chem. Soc.* **2019,** *141*, 4051-4062.
21. Huang, C.-Y.; Doyle, A. G. *J. Am. Chem. Soc.* **2012,** *134*, 9541-9544.
22. Izod, K.; Rayner, D. G.; El-Hamruni, S. M.; Harrington, R. W.; Baisch, U. *Angew. Chem. Int. Ed.* **2014,** *53*, 3636-3640.
23. Hagadorn, J. R.; Que, L.; Tolman, W. B. *Inorg. Chem.* **2000,** *39*, 6086-6090.
24. Adhikari, D.; Mossin, S.; Basuli, F.; Huffman, J. C.; Szilagyi, R. K.; Meyer, K.; Mindiola, D. J. *J. Am. Chem. Soc.* **2008,** *130*, 3676-3682.
25. Ludwiczak, M.; Majchrzak, M.; Marciniec, B.; Kubicki, M. *J. Organomet. Chem.* **2011,** *696*, 1456-1464.
26. Alberola, A.; Antolín, L. F.; Cuadrado, P.; González, A. M.; Laguna, M. A.; Pulido, F. J. *Synthesis* **1988,** *1988*, 203-207.
27. Herbert, D. E.; Lionetti, D.; Rittle, J.; Agapie, T. *J. Am. Chem. Soc.* **2013,** *135*, 19075-19078.
28. (a) Herold, S.; Lippard, S. J. *Inorg. Chem.* **1997,** *36*, 50-58; (b) Singh, A. K.; Jacob, W.; Boudalis, A. K.; Tuchagues, J.-P.; Mukherjee, R. *Eur. J. Inorg. Chem.* **2008,** *2008*, 2820-2829; (c) Sutradhar, M.; Carrella, L. M.; Rentschler, E. *Eur. J. Inorg. Chem.* **2012,** *2012*, 4273-4278; (d) Schünemann, V.; Hauke, P. Mössbauer Spectroscopy. In *Applications of Physical Methods to Inorganic and Bioinorganic Chemistry*, Scott, R. A.; Lukehart, C. M., Eds. John Wiley & Sons: West Sussex, England, 2007; pp 243-269.
29. Chilton, N. F.; Anderson, R. P.; Turner, L. D.; Soncini, A.; Murray, K. S. *J. Comput. Chem.* **2013,** *34*, 1164-1175.
30. Xue, X.-S.; Ji, P.; Zhou, B.; Cheng, J.-P. *Chem. Rev.* **2017,** *117*, 8622-8648.
31. Bordwell, F. G.; Bares, J. E.; Bartmess, J. E.; McCollum, G. J.; Van der Puy, M.; Vanier, N. R.; Matthews, W. S. *The Journal of Organic Chemistry* **1977,** *42*, 321-325.
32. Matthews, W. S.; Bares, J. E.; Bartmess, J. E.; Bordwell, F. G.; Cornforth, F. J.; Drucker, G. E.; Margolin, Z.; McCallum, R. J.; McCollum, G. J.; Vanier, N. R. *J. Am. Chem. Soc.* **1975,** *97*, 7006-7014.
33. Taskinen, E.; Nummelin, K. *The Journal of Organic Chemistry* **1985,** *50*, 4844-4847.